CaAlFe–mixed metal oxides prepared from an aluminum salt–cake and their evaluation as CO_2 sorbents at moderate temperature

Alejandro Jiménez [a], Raquel Trujillano [a], Vicente Rives [a], M.A. Soria [b,c], Luís M. Madeira [b,c], Miguel Ángel Vicente [a,*]

[a] GIR–QUESCAT, Departamento de Química Inorgánica, Universidad de Salamanca, E–37008 Salamanca, Spain
[b] LEPABE–Laboratory for Process Engineering, Environment, Biotechnology and Energy, Faculty of Engineering, University of Porto, Rua Dr. Roberto Frias, 4200–465 Porto, Portugal
[c] ALiCE–Associate Laboratory in Chemical Engineering, Faculty of Engineering, University of Porto, Rua Dr. Roberto Frias, 4200–465 Porto, Portugal

ARTICLE INFO

ABSTRACT

Potentially–CO_2 adsorbing solids at moderate temperature have been prepared by calcination at 400 °C and 750 °C of CaAlFe hydrocalumites (a sort of Ca^{2+}–layered double hydroxide), which had been prepared using a salt cake as aluminum source. The characterization of the obtained solids was carried out by powder X–ray diffraction, FT–infrared spectroscopy, thermal analysis, N_2 adsorption–desorption isotherms at –196 °C and electron microscopy. After calcination, different crystalline phases were identified as a function of the amount of Fe^{3+} incorporated. Static sorption equilibrium experiments were performed at 300 °C and $p_{CO2} = 0.3$ bar. The CO_2 sorption capacity was affected by the presence of different phases in the CaAlFe–mixed oxides (MMOs), being maximum when the amount of Fe^{3+} was 40 mol % of the trivalent positions. No differences in CO_2 sorption capacities were observed between CaAlFe–MMOs–400 and CaAlFe–MMOs–750 (materials calcined respectively at 400 and 750 °C), suggesting that CO_2 sorption capacity was not related to S_{BET}. Experiments under dynamic conditions at 400 °C and $p_{CO2} = 0.15$ bar showed good behaviors for CaAl–400, $CaAl_{0.60}Fe_{0.40}$–400 and CaFe–400. In addition, $CaAl_{0.60}Fe_{0.40}$–400 was evaluated in several CO_2 sorption–desorption cycles in the presence of water vapor, finding that the steam presence enhanced the CO_2 capture.

1. Introduction

The use of fossil fuels as the world's main source of energy is causing an increase in the concentration of carbon dioxide (CO_2) in the atmosphere [1]. CO_2 is one of the so–called greenhouse gases that contribute to global warming and climate change. The environmental effects, together with economic factors, have led the most developed countries to adopt environmental policies to reduce the risks associated to the climate change. Thus, in 2015 at the Paris Climate Conference [2], it was approved that the increase in global average temperature should be maintained at 1.5 °C with respect to temperature values prior to pre–industrial times by mid–century. In this sense, the capture and valorization of CO_2 is crucial to decrease the emissions of this gas into the atmosphere. For this purpose, several techniques have been described for the capture and separation of this gas, such as absorption, sorption, chemical loop combustion, membrane separation, hydrate–based separation, and cryogenic distillation [1]. Sorption is one of the most studied and used techniques, using a wide variety of materials: CaO–based materials [3–6], zeolites [7–9], lithium–based materials [10–14] or layered double hydroxides (LDHs) [6,15,16]. Calcined LDHs give rise to mixed metal oxides (MMOs), which, thanks to their surface basicity, are one of the families of solids with the highest CO_2 sorption capacity over a wide range of temperatures (200–400 °C), being thus suitable for pre–combustion and post–combustion applications [6,16–20]. Moreover, unlike the other materials used in CO_2 sorption, they improve their sorption capacity in the presence of steam [6,17,21], which is quite advantageous for CO_2 capture in pre–combustion and post–combustion applications.

The general formula of LDHs is $[M(II)_{1-x}M(III)_x(OH)_2]^{x+}[A_{x/n}]^{n-}\cdot mH_2O$ [22], where M(II) is a divalent cation such as Ni, Co, Cu, Mg, Mn, Ca or Zn; M(III) is a trivalent cation such as Al, Fe, Cr, Mn, V, Y or Ga; and A^{n-} is a charge balancing anion located in the interlayer space [22]. The structure of LDHs is derived from that of brucite, $Mg(OH)_2$, by a partial substitution of divalent cations (M(II)) by trivalent ones (M(III)), giving rise to positively charged layers balanced by the hydrated

* Corresponding author.
    E-mail address: mavicente@usal.es (M.Á. Vicente).

Nomenclature

List of variables

F_{CO2}	CO_2 inlet molar flow rate (mol·min^{-1})
M	Molecular mass of CO_2 (kg·mol^{-1})
m	Mass of sorbent (g)
m_i	Mass of the measuring basket (g)
m_s	mass of the activated sorbent (g)
p_{CO2}	Partial pressure of CO_2 (bar)
q	CO_2 sorption capacity (mol$_{CO2}$·kg$_{ads}^{-1}$)
q_d	CO_2 dynamic sorption capacity (mol$_{CO2}$·kg$_{ads}^{-1}$)
q_e	CO_2 equilibrium sorption capacity (mol$_{CO2}$·kg$_{ads}^{-1}$)
V_i	Volume of the measuring basket (mL)
V_s	volume of the activated sorbent (mL)
t_{test}	Total test time of sorption (min)
y_{CO2}	CO_2 molar fraction (dimensionless)

ρg	Gas density at the measuring conditions (g·mL^{-1})

List of acronyms

BET	Brunauer, Emmett and Teller method
BJH	Barrett, Joyner and Halenda method
EDS	Energy–Dispersive X–ray Spectroscopy
EGA	Evolved gas analysis
FT–IR	Fourier–Transform Infrared Spectroscopy
ICDD	International Centre for Diffraction Data
ICP–OES	Inductively coupled plasma optical emission spectrometry
IUPAC	International Union of Pure and Applied Chemistry
LDHs	Layered Double Hydroxides
MMOs	Mixed metal oxides
PXRD	Powder X–ray diffraction
SEM	Scanning electron microscopy
TEM	Transmission Electron Microscopy

anions A^{n-} [22]. Hydrocalumite is a special type of LDH. In this case, the divalent cation is Ca^{2+}, the trivalent cation is Al^{3+} and the interlayer anion is Cl^-, giving rise to a compound with the formula Ca_2Al $(OH)_6Cl\cdot 2H_2O$ [22]. Other trivalent cations such as Sc, Ga or Fe also give rise hydrocalumite compounds [23]. One of the peculiarities of this LDH is that the Ca and Al octahedra of the sheet are not randomly distributed but perfectly ordered, which results in a high crystallinity and low specific surface area compared to other LDHs [24–27]. In addition, the Ca^{2+} coordination number is 7, whereas in other LDHs the coordination number of the M(II) cations is 6 [22–24]. Hydrocalumite is used as adsorbent [28–30], antacid [31], ion exchanger [28,32] and basic heterogeneous catalyst [33–37]. Calcined hydrocalumite–type compounds, mainly composed by Ca and Al, have been used as photocatalysts in advanced oxidation processes [24,25,38] and as CO_2 adsorbents at high temperature [18,39,40]. Recently, hydrocalumite–type compounds and their calcined derivatives have been prepared using a salt cake as a source of aluminum [24–26]. Salt cake or saline slag is one of the most harmful and abundant wastes generated during secondary aluminum production [41] and it is considered a hazardous waste in Europe [42] due to its high hazardousness and toxicity for the environment and living beings. This waste can be valorized by direct application [43] or after being submitted to physico–chemical processes that allow the recovery of part of its aluminum content [41]. The preparation of value–added materials such as zeolites [44], alumina [45] or LDHs [26,46–48] using salt cake as a source of aluminum has been widely studied. On the other hand, Narayanappa and Kamath [18] have suggested that CaAl–LDHs and CaFe–LDHs hydrocalumite could be potentially interesting materials to be applied as CO_2 adsorbents, due to the synergistic effect of the presence of Fe^{3+} and Cl^- in the adsorbent, while Han et al. [49] have synthesized CaAlFe adsorbents by the sol–gel method, finding good CO_2 capture performance for promoted hydrogen production.

CaAlFe–MMOs with at least two different M(III) in the same compound have not been evaluated in CO_2 capture processes at moderate temperature. Therefore, the main novelty of this work is the evaluation of CO_2 capture by CaAlFe–MMOs containing different amounts of Fe. Moreover, pristine CaAlFe–LDHs were synthesized using aluminum from salt cake. To the best or our knowledge, there are no papers in the literature reporting on the CO_2 sorption capacity on calcined CaAlFe–LDHs.

The aim of this work is to prepare CaAlFe–LDHs materials with general formula $Ca_2Al_{1-m}Fe_m(OH)_6Cl\cdot 2H_2O$ and their calcination products (CaAlFe–MMOs) at 400 °C or 750 °C, using a saline slag as source of aluminum and incorporating variable amounts of Fe^{3+} (m = 0, 0.2, 0.4, 0.6, 0.8 and 1), and to evaluate their static CO_2 sorption capacities at moderate temperatures. Several CaAlFe–MMOs were also characterized

by cycling CO_2 breakthrough tests aiming to find an improved CO_2 capture performance by combining the sorption capacity of different phases present in the solids and the positive effect on recyclability caused by the presence of Cl^- [18]; so another aim of this work was to determine the working capacity of CaAlFe–MMOs, usually achieved after merely 3 cycles in LDH–materials [3,39,40,50].

2. Experimental

2.1. Materials

The salt cake was kindly supplied by IDALSA (Ibérica de Aleaciones Ligeras, Pradilla de Ebro, Zaragoza, Spain). NaOH (pharma grade), HCl (pharma grade, 37 %) and $FeCl_3\cdot 6H_2O$ (97–102 %) were from Panreac, while $CaCl_2\cdot 2H_2O$ (ACS 99–105 %) was supplied by Sigma Aldrich. Carbon dioxide (99.99%), nitrogen (99.999%) and helium (99.9999%) were supplied by Air Liquide. All the reagents were used as received, without any treatment. Inert silicon carbide (SiC) was supplied by Alfa Aesar and used in the breakthrough cycling tests.

2.2. Preparation of the CaAlFe mixed metal oxides

Hydrocalumite and Fe^{3+}–doped hydrocalumite were prepared following the methodology recently reported [25,26]. Salt cake was treated in basic media under optimal conditions (as reported previously) [41], and the obtained aluminum solution was then used to carry out the synthesis of the CaAlFe–LDHs by the coprecipitation method, according to the methodology described elsewhere [25].

Synthetic hydrocalumite samples were named as $CaAl_{1-m}Fe_m$, where *m* stands for the amount of Fe^{3+} incorporated into the hydrocalumite–type solid, expressed as molar fraction of the trivalent cations. To evaluate the effect of the calcination temperature in the CO_2 capture capacity, samples CaAl, $CaAl_{0.80}Fe_{0.20}$, $CaAl_{0.60}Fe_{0.40}$, $CaAl_{0.40}Fe_{0.60}$, $CaAl_{0.20}Fe_{0.80}$ and CaFe were calcined in air atmosphere at a heating rate of 10 °C/min from room temperature to 400 °C, and once this temperature was reached, it was maintained for 2 h, and then the furnace was turned off, leaving the sample to return to room temperature. On the other hand, samples CaAl, $CaAl_{0.80}Fe_{0.20}$, $CaAl_{0.60}Fe_{0.40}$ and CaFe were calcined at 750 °C using the same heating rate and calcination time as in the calcination at 400 °C. These temperatures were selected taking into account the results reported in the literature [51] and in our previous studies [24,25,52]. To name the calcined solids, the calcination temperature, in Celsius, was added to the name of the uncalcined samples.

2.3. Characterization techniques

A Siemens D–5000 equipment was used to record the powder X–ray diffraction (PXRD) patterns of the samples (λ = 0.154 nm Cu–Kα radiation, fixed divergence, 5°–70° (2θ), scanning rate 2°(2θ)/min, 0.05° steps, 1.5 s/step). The crystalline phases formed were identified by comparison with the JCPDS–International Centre for Diffraction Data Database (ICDD®) [53].

The FT–IR spectra were recorded in a Perkin–Elmer Spectrum Two instrument with a nominal resolution of 4 cm^{-1} from 4000 to 400 cm^{-1}, using KBr (Merck, grade IR spectroscopy) pressed pellets and averaging 20 scans to improve the signal–to–noise ratio.

Element chemical analyses for Ca, Fe, Al and Si were carried out by Inductively Coupled Plasma Mass Spectrometry (ICP–MS) in an ICP–MS apparatus model Agilent 7800. Digestion was carried out in acid medium, in a closed Teflon vessel. Concentrated HNO$_3$ was used as a reagent, bringing the final solution to 50 mL. For the digestion a Milestone Microwave equipment model ULTRAWAVE with temperature and pressure control was used (Nucleus Research Platform, University of Salamanca, Spain).

The thermogravimetric (TG) curves were recorded in a SDT Q600 apparatus (TA Instruments) at a heating rate of 5 °C/min up to 900 °C under nitrogen (Air Liquide, Spain, 99.999 %) flow (50 mL/min). Approximately 10 mg of sample were used to perform the analyses. The gaseous and vapor species formed during the thermal decomposition were analyzed (EGA, evolved gas analysis) by a mass spectrometer (Pfeiffer Vacuum ThermoStar TG–MS) connected to the thermal analysis equipment.

The N$_2$–adsorption–desorption isotherms were recorded at –196 °C using a Micromeritics Gemini VII 2390 T equipment. Prior to analysis, N$_2$ was flowed through the sample (*ca.* 0.1 g) at 110 °C for 2 h to remove weakly adsorbed species. The specific surface areas were calculated by the Brunauer–Emmet–Teller (BET) [54,55] method and the average pore diameters by the Barrett–Joyner–Halenda (BJH) method applied to the desorption branch of the isotherm [55,56].

Scanning electron microscopy (SEM) images were obtained using a JEOL IT500 Scanning Electron Microscope equipped with an Energy–Dispersive X–ray spectroscopy (EDS) microanalysis accessory, and the Transmission Electron Microscopy (TEM) images using a Tecnai Spirit Twin in 120 kV Transmission Electron Microscope, both at the Nucleus Research Platform (University of Salamanca, Spain).

2.4. Sorption studies

It is worth mentioning that, for the same material under the same conditions, the CO$_2$ sorption capacities determined from static and dynamic methods were similar (difference of less than 10% – data not shown for brevity). In post–combustion processes the p_{CO2} ranges between 0.03 bar and 0.2 bar (concentration between 3% and 20 %), while in pre–combustion processes the composition ranges between 15 and 60 % at higher pressures [57]. Taking into account these data reported in the literature, p_{CO2} pressures of 0.15 bar (dynamic experiment) and 0.30 bar (static experiment) were chosen.

2.4.1. Static experiments

The CO$_2$ static tests were carried out by the gravimetric method on a CI Precision Microbalance with a precision of $\pm$ 0.001 mg using a gas sorption analyzer (model GHP–50 Sorption Analyzer from VTI Corporation), which is limited to operation up to 300 °C. Before introducing the sample into the CI microbalance, an ex–situ calcination was done at 400 or 750 °C for 2 h, yielding the CaAlFe–MMOs.

Static equilibrium sorption capacity was calculated by the specific amount of gas sorbed (q_e), given by Eq. (1):

$$q_e = \frac{\Delta m + (V_s + V_i)\rho_g}{m_s M} \tag{1}$$

where $\Delta m = m - m_s - m_i$; m is the mass measured by de microbalance during CO$_2$ static tests; m_s and V_s are the mass and volume of the activated sorbent, respectively, measured at 300 °C and under vacuum; m_i and V_i are the mass and volume of the measuring basket, respectively, calculated by helium picnometry; ρ_g is the gas density at the measuring conditions and M is the molecular mass of CO$_2$. Therefore, equation (1) includes the correction of the buoyancy effect. A typical experiment started by degassing the CaAlFe–MMOs sample (55 mg) at 300 °C and under vacuum ($\approx$ 0.001 bar) for 1 h to remove any adsorbed atmospheric CO$_2$ and water. Afterwards, the activated sample was cooled down to 100 °C under vacuum and the solid density determined in–situ by helium picnometry. Finally, the sample was warmed up again to 300 °C and the initial mass of the activated sample (m_s) was recorded. When temperature stabilized ($\pm$2 °C), CO$_2$ was fed to the chamber until reaching the target pressure of 0.3 bar. The samples were allowed to stand under such conditions until almost no variation was observed on the sample mass (lower than 0.03 mg in 30 min). The maximum duration of the experiments was 18 h, which is the necessary time to reach the equilibrium. The sample that presented the best behavior was then submitted to 6 successive CO$_2$ sorption–desorption cycles, each cycle lasting 1.5 h (1 h sorption and 0.5 h desorption). The CO$_2$ pressure was kept at 0.3 bar during sorption, while the vacuum pump was used during desorption to reach a pressure of 0.001 bar; the experiments were carried out at 300 °C.

2.4.2. Dynamic experiments

The experimental setup used in the dynamic experiments has already been described in previous works [17,58]. This set–up consists of a steel column that is introduced into a tubular furnace (model Split from Termolab, Fornos eléctricos, Lda.) equipped with a 3–zone PID temperature controller (model MR13 from Shimaden). The gases (CO$_2$ and N$_2$) were fed by mass flow controllers (from Bronkhorst High–Tec) and the target content of water in the feed was achieved by using a Controlled Evaporator Mixer (CEM). The outlet dry composition of CO$_2$ was recorded with an on–line infrared CO$_2$ analyzer (Servomex, model 4210). The vapor was condensed using a Peltier cold trap located between the sorption column outlet and the analyzer. Blank measurements, using the same CO$_2$ composition and filling the column only with an inert material (SiC), were made to estimate the residence time in the tubes and eliminate it in the calculated sorption capacities.

The steel column (120 mm of height and 7.2 mm of inner diameter) was filled with approximately 0.8 g of SiC in both ends and 1 g of the samples (200–300 μm), namely CaAl–400, CaAl$_{0.60}$Fe$_{0.40}$–400 or CaFe–400, in the middle. The steel column was closed in both ends with stainless steel mesh discs (10–15 μm). The CO$_2$ breakthrough runs were carried out at 400 °C, atmospheric pressure and a total flow rate of 100 mL$_N$/min of gaseous mixture. For the CO$_2$ sorption experiments the inlet stream contained 15 vol% CO$_2$ and 85 vol% N$_2$, while for the CO$_2$ sorption experiments in the presence of water the composition of the inlet stream was 15 vol% CO$_2$, 15 vol% H$_2$O and 70 vol% N$_2$; for the desorption experiments the inlet stream was composed of pure N$_2$. Before submitting the CaAlFe–MMOs to the breakthrough experiments, an in–situ activation treatment at 400 °C under a N$_2$ atmosphere for 1 h was carried out. Each sample tested was submitted to five successive sorption–desorption cycles, ending the sorption step when the amount of CO$_2$ at the outlet was the same as at the inlet, and ending the desorption step when the variation of CO$_2$ concentration at the outlet was constant and lower than 0.05 vol%.

Sorption capacity of the samples in the dynamic tests (q_d) was calculated using equation (2):

$$q_d = \frac{F_{CO_2}^{in} \int_0^{t_{test}} \left(1 - \frac{y_{CO_2}^{out}}{y_{CO_2}^{in}}\right)dt}{m_s} \tag{2}$$

where $F_{CO_2}^{in}$ is the CO$_2$ inlet molar flow rate, t_{test} is the total test time of

sorption, $y_{CO_2}^{out}$ and $y_{CO_2}^{in}$ are the CO_2 outlet and inlet molar fractions (dry basis), respectively, and m_s is the mass of the sorbent. It is important to underline that the dead volume (determined by the blank tests performed by filling the column only with SiC) was taken into account to apply Eq. (2).

3. Results and discussion

3.1. Extraction of aluminum

The extraction conditions reported in our previous works [24–26,41] allowed to obtain a pure aluminum solution suitable for the synthesis of CaAlFe–LDHs by coprecipitation.

3.2. Characterization of the solids

All the as–synthesized samples showed a layered structure characteristic of hydrocalumite LDH–type compounds (ICDD card 01–072–4773) (Fig. S1). As mentioned above, hydrocalumite is a sort of LDH containing Ca^{2+}, whose radius (100 pm) is much larger than that of Mg^{2+} (72 pm) [59], which forms hydrotalcite (MgAl–LDH). This larger size of Ca^{2+}, together with the fact that its coordination number in hydrocalumite is 7 (as a water molecule from the interlayer space coordinates to Ca^{2+}), means that the Ca and Al octahedra are not randomly distributed as with the Mg and Al octahedra in hydrotalcite, but are distributed in a perfectly ordered manner, resulting in a higher crystallinity of hydrocalumite with respect to other LDHs. Al^{3+} can be isomorphically replaced by other trivalent cations such as Fe^{3+} or Ga^{3+} [23–25]. When Al^{3+} is isomorphically replaced by a larger radius M(III) cation, a decrease in crystallinity occurs [23,24], because there is a decrease in the radius difference between those of the divalent and the trivalent cations, which is related to the crystallinity [23,24]. Fig. S1 shows the X–ray patterns of the starting, uncalcined, CaAlFe–LDHs, in which a decrease in crystallinity was observed as the aluminum content decreased, in agreement with the literature [24,25]. No additional crystalline phases were identified in addition to the hydrocalumite–type phase.

The thermal behavior of the synthesized CaAlFe–LDHs, which was discussed in detail in previous works [24,25,52], is summarized in Fig. S2. The thermal decomposition sequence of hydrocalumite–type compounds can be divided into three stages: dehydration (below 180 °C), dehydroxylation of the sheets (between 180 and 400 °C), and decarbonation and/or completion of the dehydroxylation process (between 400 and 750 °C) [52]. Considering this behavior, the temperatures of 400 °C and 750 °C were selected to calcine the CaAlFe–LDHs to obtain the corresponding CaAlFe–MMOs to evaluate their CO_2 capture capacities.

3.2.1. Calcined solids

The powder X–ray diffractograms of the samples calcined at 400 °C are shown in Fig. 1A. In all cases, the layered structure was no longer observed, leading to the formation of amorphous mixed oxides. In samples $CaAl_{0.60}Fe_{0.40}$–400, $CaAl_{0.40}Fe_{0.60}$–400 and $CaAl_{0.20}Fe_{0.80}$–400, a diffraction peak at 29.4° characteristic of calcite ($CaCO_3$, ICDD 01–072–1937) was observed; calcite can be formed by fixation of atmospheric CO_2, although the diffractograms were recorded immediately after the calcination treatment, once the sample reached room temperature. In samples with larger Fe^{3+} content ($CaAl_{0.40}Fe_{0.60}$–400, $CaAl_{0.20}Fe_{0.80}$–400 and CaFe), broad and weak diffraction peaks corresponding to magnetite (Fe_3O_4, ICDD card 01–072–6170) and hematite (Fe_2O_3, ICDD card 01–084–0311) were observed. On the contrary, in samples with low Fe^{3+} content, no crystalline phases were observed.

The powder X–ray diffractograms of the samples calcined at 750 °C are shown in Fig. 1B. The main difference with respect to the samples calcined at 400 °C is that the calcination products at 750 °C were highly crystalline, which could affect the CO_2 capture capacity of the CaAl-Fe–MMOs. Thus, when the starting material was $Ca_2Al(OH)_6Cl·2H_2O$ (sample CaAl–750), the phases detected by PXRD were mayenite ($Ca_{12}Al_{14}O_{33}$, ICDD card 01–070–2144), calcium hydroxychloride (CaClOH, ICDD card 01–073–1885) and calcium oxide (CaO, ICDD card 01–070–5490). No other crystalline phases were detected. As Al^{3+} was replaced by Fe^{3+}, the phases detected in the calcination products were different. When 20% of the Al^{3+} was replaced by Fe^{3+}, in addition to mayenite, CaClOH and CaO, a new phase was observed: Ca_2FeO_3Cl (ICDD card 01–071–1437). When 40% Al^{3+} was replaced by Fe^{3+}, the formation of an additional Ca–Fe phase was also observed: srebrodolskite ($Ca_2Fe_2O_5$, ICDD card 01–074–3658), in addition to mayenite, CaClOH, CaO and Ca_2FeO_3Cl. An important difference of this sample with respect to the other samples calcined at 750 °C was that a diffraction peak characteristic of calcite ($CaCO_3$) was recorded at 29.4°, calcite being formed by atmospheric CO_2 fixation. Finally, when the Al^{3+} was completely replaced by Fe^{3+} (sample CaFe–750), formation of mayenite and CaO was not observed, but the presence of srebrodolskite ($Ca_2Fe_2O_5$) and Ca_2FeO_3Cl, as well as CaClOH, was detected (although the identification of this last phase was complicated due to the broadness and overlapping of the diffraction peaks of the different phases in this sample). The phases identified in the CaAlFe–LDHs calcination products agreed with data in the literature [24,60].

Fig. S3 shows the FT–IR spectra of the samples calcined at 400 °C (Fig. S3A) and 750 °C (Fig. S3B). All of them were very similar to each other and without major differences between the samples calcined at different temperatures, showing a broad band in the 3600–3400 cm^{-1} range due to the overlapping of the bands of the stretching vibrations of the hydroxyl groups in different environments [19]. The presence of water molecules was confirmed by the band at 1637 cm^{-1}. The bands at 1413 cm^{-1} and 873 cm^{-1} confirmed the presence of carbonate in the
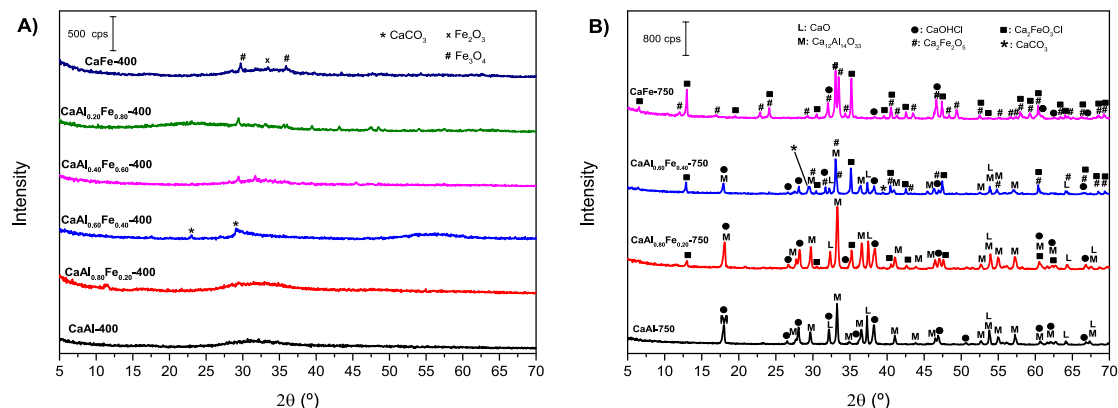

Fig. 1. Powder X–ray diffraction patterns of samples calcined at 400 °C (A) and 750 °C (B).

samples, which was formed by the fixation of atmospheric CO_2 due to the basic character of the MMOs [18,19,36], although the FT–IR spectra were recorded immediately after the calcination process, once the sample reached room temperature. The band at 806 cm^{-1} was recorded in the spectra of the high Al^{3+}–content containing samples and decreased as the amount of Fe^{3+} in the samples increased, so it could be attributed to the Al—OH bond, although band assignment in this range of the IR spectrum was extremely complicated due to the broadness and overlapping of the bands. The bands due to M—OH bonds, where M can be Ca^{2+}, Al^{3+} or Fe^{3+}, were recorded in the 700 to 400 cm^{-1} range [19].

The nitrogen sorption–desorption isotherms of the solids calcined at 400 °C and 750 °C are shown in Fig. S4. According to the IUPAC criteria [55], all isotherms were of type II. Only the curves for samples $CaAl_{0.20}Fe_{0.80}$–400, CaFe–400, $CaAl_{0.60}Fe_{0.40}$–750, $CaAl_{0.40}Fe_{0.60}$–750 and CaFe–750 showed very narrow hysteresis cycles, which, according to the IUPAC criteria, are of type H3. Table 1 shows the BET specific surface area (S_{BET}) values for the uncalcined samples and for the samples calcined at 400 and 750 °C. The S_{BET} values of the uncalcined samples agreed with the PXRD data (Fig. S1), so that an increase in Fe^{3+} content implied a decrease in crystallinity, and consequently an increase in S_{BET}. When the samples were calcined at 400 °C, the layered structure disappeared, and part of the water molecules were removed. However, the calcination process did not produce an increase in S_{BET} as usually occurs with other LDHs [58], but rather a decrease in S_{BET}, possibly associated to the collapse of the layered structure and the formation of microcrystallites that can block the access of the N_2 molecules to the porosity network [25]. Calcination of CaAlFe–LDHs at 750 °C implied a decrease in S_{BET} with respect to the starting LDHs and to the products calcined at 400 °C, since at 750 °C high crystallinity solids were obtained. The S_{BET} values of the samples used in this work agreed with those reported in the literature for this type of solids [24,25,36]. On the other hand, the average pore width remained in the mesopore range for samples calcined at 400 °C and 750 °C.

Fig. 2A and Fig. S5A–C show SEM micrographs of the CaAl–400 sample. The presence of particle aggregates of size 60–70 μm, consisting of hexagonal shaped particles [25], was observed. The hexagonal–shaped particles are characteristic of LDH–type compounds, and showed that calcination at 400 °C did not completely destroy the layered structure of the starting CaAlFe–LDHs [25,47,61]. In addition, sintering of the hexagonal plate–shaped particles was observed. As the Fe^{3+} content increased, the plate–shaped particles began to lose the hexagonal shape, becoming rounded plates until the total substitution of Al^{3+} by Fe^{3+} occurred, when the presence of small irregularly shaped particles and aggregates of particles with a spongy appearance was observed (Fig. 2F and Fig. S5P–R). Fig. 2B and Fig. S5,D–F show SEM micrographs of the $CaAl_{0.80}Fe_{0.20}$–400 sample, whose morphology and appearance were like those observed in the CaAl–400 sample, although the particle aggregates showed a smaller size and small lamellae appear to be of a small size. The SEM micrographs for samples $CaAl_{0.60}Fe_{0.40}$–400 and $CaAl_{0.40}Fe_{0.60}$–400 were similar to each other (Fig. 2C and 2D and Fig. S5G–I and J–L, respectively), with aggregates of particles of size

approximately 50 μm with a shape of small lamellae, smaller than in the CaAl–400 CaAl$_{0.80}$Fe$_{0.20}$–400 samples. Finally, in Fig. 2E and 2F and in Fig. S5M–O and S5P–R, SEM micrographs of the $CaAl_{0.20}Fe_{0.80}$–400 and CaFe–400 samples, respectively, are shown; particle aggregates between 30 and 40 μm, made up of irregularly shaped particles, were observed. The appearance of higher sponginess as the Fe^{3+} content increased in the CaAlFe–MMO could justify the slight increase in S_{BET} values (Table 1). Fig. S6 shows the results of the EDS analysis of the $CaAl_{0.60}Fe_{0.40}$–400 sample, with appreciable carbon content, which was likely to come from the fixation of atmospheric CO_2 due to the high capacity of this sample to capture this gas (see below).

Fig. S7A–C show SEM micrographs of sample CaAl–750, wherein aggregates with a size between 60 and 80 μm and a smooth surface are observed. In Fig. 2G SEM micrograph of CaAl–750 with high magnification is shown. Aggregates of hexagonal plate–shaped particles with rounded corners were observed, clearly different with respect to the same sample calcined at 400 °C; a higher degree of sintering was also observed. However, the $CaAl_{0.80}Fe_{0.20}$–750 sample SEM micrographs (Fig. S7D–F) show a very different appearance from CaAl–750, being composed of much smaller particle size aggregates (20–30 μm). The particles forming these aggregates have a certain hexagonal shape. When magnification is increased (Fig. 2H), small flake–shaped particles are observed, with a certain rough appearance. This aspect is also different from that observed in the same sample when calcined at 400 °C, where very small particles with hexagonal shape and rounded corners were observed.

Fig. S7G–H show SEM micrographs of the $CaAl_{0.60}Fe_{0.40}$–750 sample. In this case, particle aggregates of size 50–70 μm were found, consisting of irregularly shaped particles with a flaky appearance. When the magnification is increased (Fig. 4I and S7I), particles with a certain hexagonal shape and with a certain flaky appearance in the form of a thin plate were observed. It is also important to note that the particles present a much smaller thickness compared to CaAl–750 and $CaAl_{0.80}Fe_{0.20}$–750 samples. Fig. S8 shows the results of the EDS analysis, where a high carbon content was observed in the $CaAl_{0.60}Fe_{0.40}$–400 sample, which could come from the fixation of atmospheric CO_2 during the handling of the sample, due to its high capacity to capture this gas. Finally, the SEM micrograph of the CaFe–750 sample is shown in Fig. S7J where aggregates of particles close to 100 μm in size and irregular in shape were found, with a smoother and less porous appearance than the rest of the samples calcined at 750 °C. Fig. 2J, S7K and S7L show SEM micrographs at higher magnification, showing particles of an even smaller size than in the rest of the samples calcined at 750 °C, where the flake–like hexagonal shape has been practically lost to give rise to particles with a more rounded appearance and a higher degree of sintering. With increasing Fe^{3+} content in CaAlFe–MMOs–750, a decrease in flake particle size and thickness was observed. In addition, a loss of the hexagonal shape of the plate–shaped particles was also observed, giving rise to particles with a more rounded appearance and with a higher degree of sintering. The appearance of the particle aggregates also varies with increasing Fe^{3+} content, with more compact aggregates being observed with smaller voids or channels and with a rougher appearance, which could justify the slight increase in S_{BET} and decrease in pore size observed with increasing Fe^{3+} content in the samples calcined at 750 °C.

Two TEM micrographs of the $CaAl_{0.60}Fe_{0.40}$–400 sample are included in Fig. 3A and 3B. Aggregates of hexagonal–shaped particles with slightly rounded corners spherical shaped were observed in Fig. 3A, with some degree of sintering. In the higher magnification micrograph (Fig. 3B), the size of hexagonal–shaped particles was approximately 70–90 μm in diameter, and the degree of sintering between these particles was observed in greater detail. In this case, the particles seemed not to be hollow. This agrees with literature data for this type of samples when calcined at 400 °C, i.e. the hexagonal plate–shaped particles are not destroyed [25,47,61]. Fig. 3C and 3D show two TEM micrographs of sample $CaAl_{0.60}Fe_{0.40}$–750. Aggregates of particles were observed in the

Table 1
S_{BET} (m^2/g) and average pore diameter (nm) values of samples uncalcined and calcined at 400 and 750 °C.

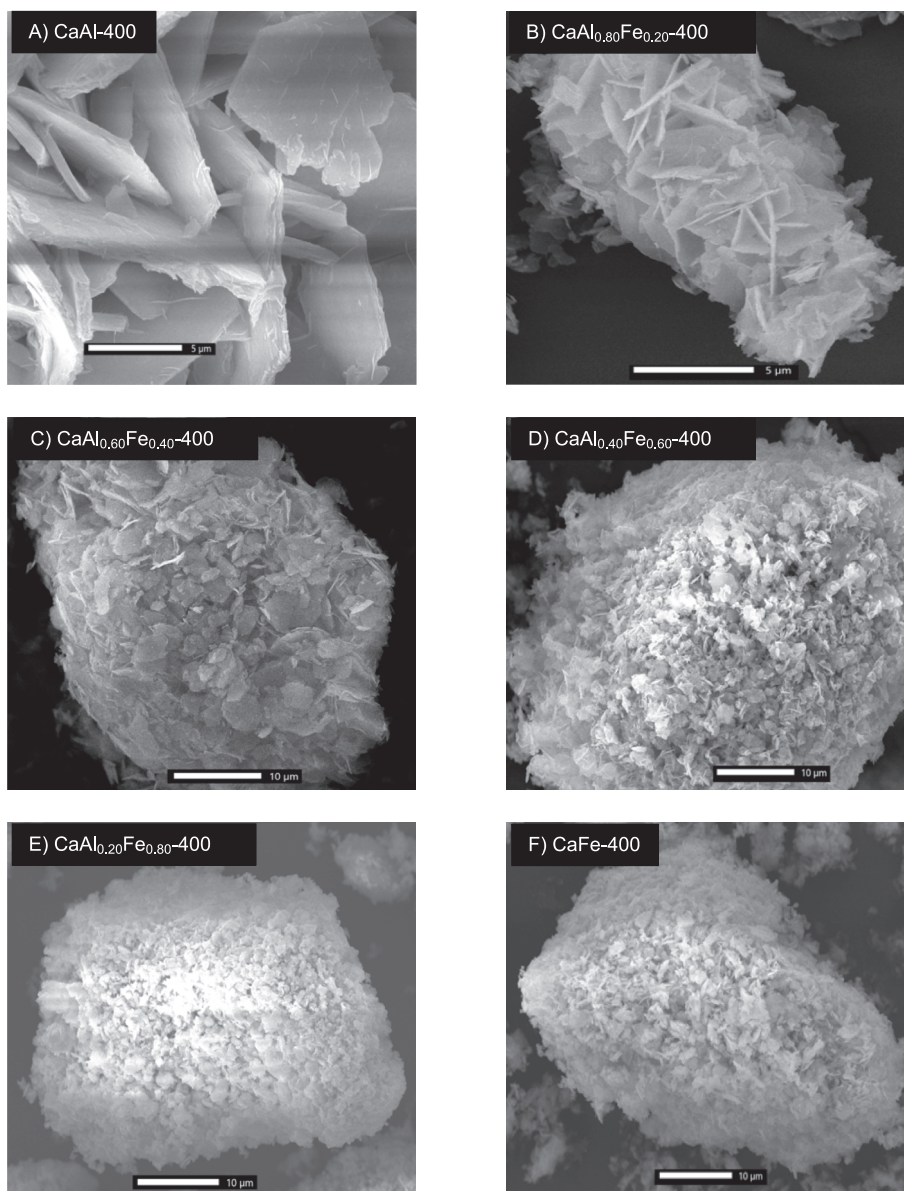| Sample	Non–calcined [25]		Calcined at 400 °C		Calcined at 750 °C	
	S_{BET}	Average Pore Diameter	S_{BET}	Average Pore Diameter	S_{BET}	Average Pore Diameter
CaAl	12	8.7	5	5.5	3	8.3
$CaAl_{0.80}Fe_{0.20}$	20	8.2	16	9.9	7	7.8
$CaAl_{0.60}Fe_{0.40}$	22	8.9	10	8.2	7	9.5
$CaAl_{0.40}Fe_{0.60}$	28	9.0	12	8.5	*	*
$CaAl_{0.20}Fe_{0.80}$	32	8.2	10	10.0	*	*
CaFe	27	9.3	16	10.1	7	7.6

*Not determined.

Fig. 2. SEM micrographs of the samples calcined at 400 °C and 750 °C.

form of hexagonal plates with rounded corners between which a certain degree of sintering was observed. The size of the particles forming the aggregates was smaller than for the same sample but calcined at 400 °C, although the size of the particle aggregates appeared to be slightly larger, as well as the degree of sintering was also higher in the sample calcined at 750 °C than in that calcined at 400 °C. The higher degree of sintering could justify the fact that the particle aggregates were larger in the sample calcined at 750 °C.

3.3. CO₂ sorption experiments

3.3.1. Static experiments

Fig. 4 shows the equilibrium CO_2 sorption capacity of the CaAl-Fe–LDH samples calcined at 400 °C. The lowest performance is shown by sample CaAl$_{0.80}$Fe$_{0.20}$–400 °C, whose sorption capacity was lower than 0.3 mol$_{CO2}$·kg$_{ads}^{-1}$, the value taken as the low limiting that a material must show to be applied in CO₂ capture in pre–combustion [19,20]. The sorption capacities for the other samples were higher than 0.3 mol$_{CO2}$·kg$_{ads}^{-1}$. It is important to highlight that, as Al^{3+} was

isomorphically replaced by Fe^{3+}, there was an improvement in the sorption capacity of the samples (except for CaAl$_{0.80}$Fe$_{0.20}$–400), sample CaAl$_{0.60}$Fe$_{0.40}$–400 reaching the highest CO₂ sorption capacity. Then, by increasing the Fe^{3+} content to 60 and 80 %, the sorption capacity of these samples remained at values much higher than that of the CaAl–400 sample (close to twice), but lower than that for CaAl$_{0.60}$Fe$_{0.40}$–400, and slightly higher than that for CaFe–400 sample. Data in Fig. 4 suggested the presence of two different CO₂ sorption mechanisms in CaAlFe–MMOs–400, one for low Fe^{3+} contents and the other for high Fe^{3+} contents (see discussion on this point below).

Considering the behavior of the CaAlFe–MMOs–400 samples, CaAl, CaAl$_{0.80}$Fe$_{0.20}$, CaAl$_{0.60}$Fe$_{0.40}$ and CaFe samples were calcined at 750 °C and their CO₂ sorption behaviors were evaluated under the same conditions (at 300 °C and 0.3 bar CO₂). Fig. 5 shows the equilibrium CO₂ sorption capacities of samples CaAlFe–MMOs–750. Again, the sample showing the highest q_e value was CaAl$_{0.60}$Fe$_{0.40}$–750 (q_e = 1.58 mol$_{CO2}$·kg$_{ads}^{-1}$), followed by samples CaFe–750 (q_e = 0.84 mol$_{CO2}$·kg$_{ads}^{-1}$) and CaAl–750 (q_e = 0.52 mol$_{CO2}$·kg$_{ads}^{-1}$). Finally, sample CaAl$_{0.80}$Fe$_{0.20}$–750 had the lowest q_e value (0.27 mol$_{CO2}$·kg$_{ads}^{-1}$). For
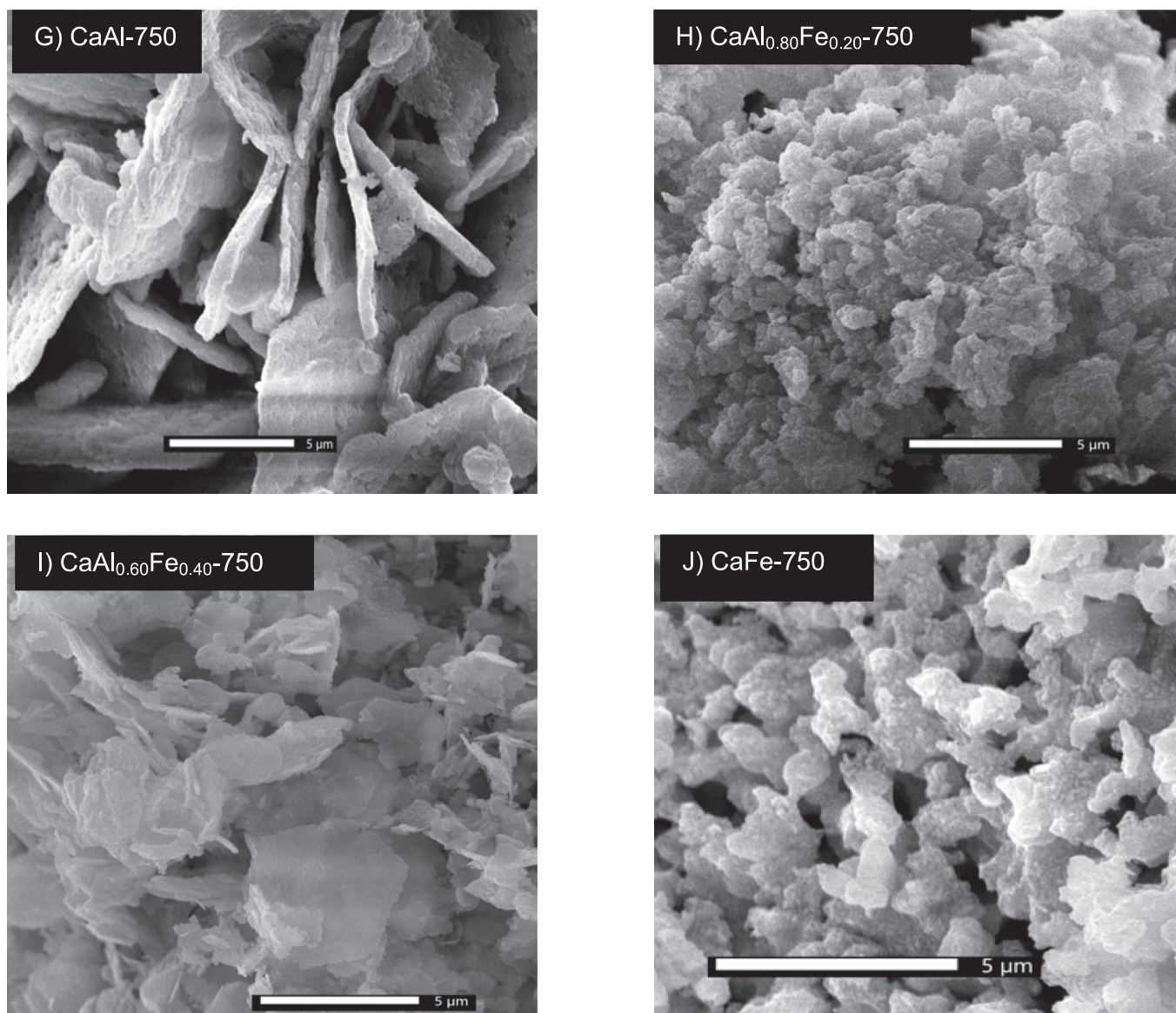
Fig. 2. (*continued*).

comparison, Fig. 5 also includes the sorption capacities of the samples calcined at 400 °C; the sorption capacities remained practically unchanged when the calcination temperature of the CaAlFe–LDHs samples was raised from 400 °C to 750 °C. Similar q_e values at both calcination temperatures suggest that the S_{BET} of the samples was not a determinant parameter on their CO_2 sorption capacities, as reported by other authors for other MMOs derived from LDHs [20,62]. Increasing the calcination temperature led to a decrease in S_{BET} (Table 1). According to literature [51], the appearance of crystalline phases and the sintering of the adsorbents is favored as the calcination temperature of LDHs increases, resulting in a decrease of S_{BET}. On the other hand, with the calcination temperature increase, the number and strength of the basic sites of the calcined materials increase [39,63,64]; there is a temperature (400 °C) where the trade–off of both factors is optimum [51].

Furthermore, as in the case of the CaAlFe–MMOs–400 samples, the existence of two different ways of CO_2 sorption was observed, one for high Al^{3+} content and the other for high Fe^{3+} content, with a synergistic effect when the Al^{3+}/Fe^{3+} molar ratio is close to 1. Up to the authors' knowledge, only Narayanappa et al. [18] have studied the sorption of CO_2 on calcined CaAl–LDHs and on CaFe–LDHs, reporting that on CaAl–MMOs sorption took place through CaO dispersed on mayenite

and $Ca_2Fe_2O_5$ forming $CaCO_3$, but they did not study the sorption on mixed CaAlFe–MMOs. On the other hand, CO_2 sorption on CaAl–MMOs and/or on CaO or dispersed CaO has been widely reported, but always at temperatures above 600 °C [3,5].

As mentioned above, data in Figs. 4 and 5 and PXRD results in Fig. 1 suggest that CO_2 sorption on CaAlFe–MMOs proceeded through two different mechanisms, depending on the relative amounts of Al^{3+} and Fe^{3+}, with a synergistic effect for the $CaAl_{0.60}Fe_{0.40}$ sample. In samples whose Al^{+3} content is high, the CO_2 capture would take place through CaO, as reported in the literature [3,39,40]. The thermal decomposition of hydrocalumite has been widely studied [3,39,52], with mayenite ($Ca_{12}Al_{14}O_{33}$), CaO and CaOHCl being reported as final phases of the thermal decomposition below 1000 °C. From the point of view of CO_2 capture, mayenite acts as an inert support on which the adsorbent phase, CaO, is dispersed [3,5,18,40]. Mayenite avoids the sintering of CaO, thus improving the adsorbate behavior in cyclic carbonation–decarbonation processes [3,5,18,40]. In addition, the CaO/mayenite ratio affects the CO_2 capture capacity of the adsorbent [5]. In this work, as observed in Fig. 1, the samples with high Al^{3+} content and calcined at 750 °C (CaAl–750 and $CaAl_{0.80}Fe_{0.20}$–750) were constituted by crystalline mayenite, CaO, CaOHCl and Ca_2FeO_3Cl (the presence of other
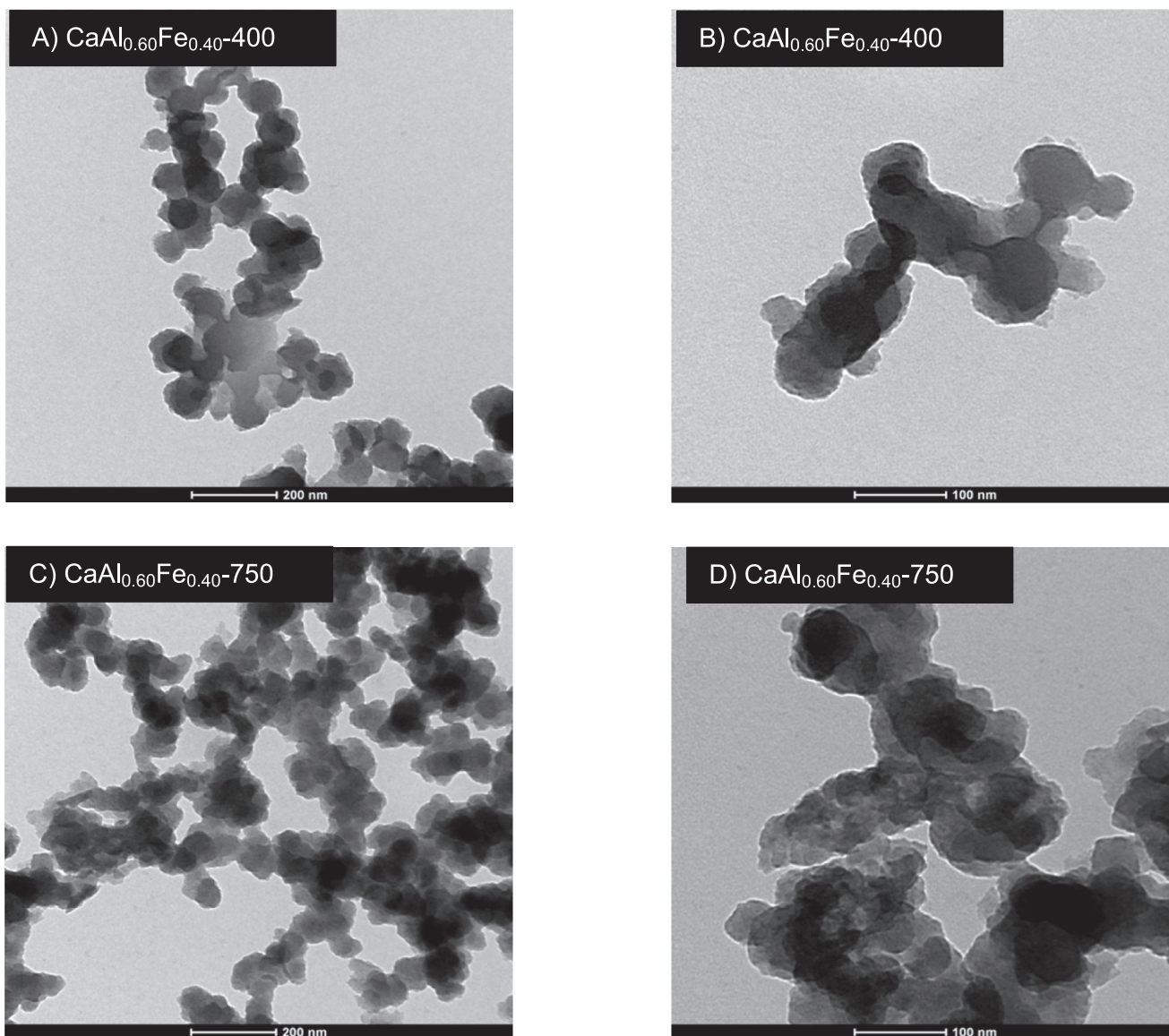
Fig. 3. TEM micrographs of $CaAl_{0.40}Fe_{0.60}$ sample calcined at 400 °C (A and B) and calcined at 750 °C (C and D).

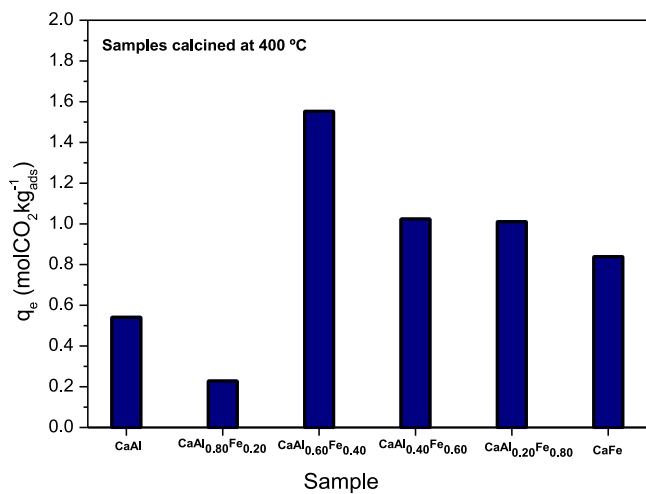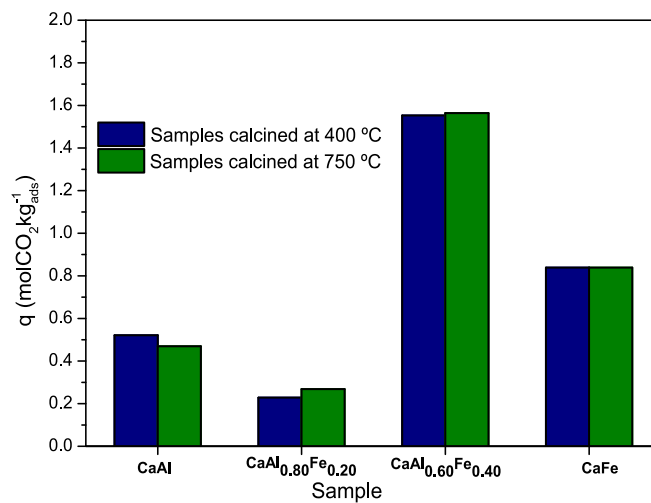**Fig. 4.** CO_2 sorption capacity of CaAlFe–LDHs calcined at 400 °C under p_{CO2} = 0.3 bar and 300 °C.

Fig. 5. CO_2 sorption capacity of samples CaAlFe–LDHs calcined at 400 and 750 °C under p_{CO2} = 0.3 bar and 300 °C.

amorphous phases cannot be completely ruled out). In these samples, sorption was expected to take place through CaO, forming $CaCO_3$, and to a lesser extent also through CaOHCl, which was dispersed on mayenite in the case of sample CaAl–750. It was expected that by replacing 20% of Al^{3+} by Fe^{3+}, the amount of mayenite in the final solid would decrease, since Fe^{3+} did not replace Al^{3+} in mayenite nor did it form an analogous oxide with Ca^{2+} [24]. By decreasing the relative amount of mayenite, the amount of CaO segregated should increase; however, this did not occur, because Fe^{3+} reacted with Ca^{2+} to form the Ca_2FeO_3Cl phase, which is inert for CO_2 sorption. Then, CaO would be dispersed over two different phases and the content in the final adsorbent would be lower. This could justify why when replacing 20% of Al^{3+} by Fe^{3+} a loss of CO_2 capture capacity of the adsorbent CaAl$_{0.80}$Fe$_{0.20}$–750 with respect to CaAl–750 was observed (Figs. 4–5).

At the opposite extreme, when practically all Al^{3+} was replaced by Fe^{3+}, formation of the Ca_2FeO_3Cl and $Ca_2Fe_2O_5$ phases was observed in sample CaFe–750 (Fig. 1); formation of crystalline CaO was not observed in this sample, as for all other samples calcined at 750 °C, therefore the calcite identified by PXRD after using this sample in CO_2 capture could not come from the reaction of CaO with CO_2. However, the non-identification of CaO by PXRD did not undoubtedly imply the absence of this phase, as low content and/or small size of CaO crystallites may difficult its identification by PXRD. In any case, if the mineralogical composition determined by PXRD is considered, the active phase with respect to CO_2 sorption was expected to be $Ca_2Fe_2O_5$. As

reported by Gupta et al. [65], $Ca_2Fe_2O_5$ can adsorb CO_2 also yielding $CaCO_3$, through the reversible reaction: $Ca_2Fe_2O_5(s) + 2CO_2(g) \leftrightarrow 2CaCO_3(s) + Fe_2O_3(s)$. In the case of the CaAl$_{0.60}$Fe$_{0.40}$–750 sample, which showed the highest q_e value for both series of samples calcined at 400 °C and 750 °C, two phases active on CO_2 sorption were identified from the phase composition of the materials shown in Fig. 1: CaO and $Ca_2Fe_2O_5$. In this case, both phases would be dispersed on a matrix of mayenite and Ca_2FeO_3Cl. The optimum phase/support ratio would occur in this sample; at low Fe^{3+} contents the presence of $Ca_2Fe_2O_5$ was not observed and at high Fe^{3+} contents the CaO content would decrease. At each end of the series, a single phase responsible for CO_2 sorption was present: CaO at high Al^{3+} content and $Ca_2Fe_2O_5$ at high Fe^{3+} content. If this hypothesis is right for CO_2 sorption on the high and low Al^{3+} samples, the diffraction peaks corresponding to $CaCO_3$ would be observed in the PXRD diffractograms of the used solids (see section 3.4 below).

This mechanism for CO_2 capture using CaAlFe–MMOs proceeds through formation of $CaCO_3$, which is one of the main limitations of CaO–based CO_2 adsorbents in cyclic processes [3,5,18,40], due to the high temperature (above 700 °C) required to regenerate the adsorbent, through the reaction $CaCO_3(s) \rightarrow CaO(s) + CO_2(g)$. Another disadvantage of CaO–based adsorbents in cyclic processes is the sintering of the active phase particles, which is favored by the high temperatures that are used for CO_2 sorption by CaO–based materials [3,5,18,40]. This could lead to the conclusion that CaAlFe–MMOs could present a bad
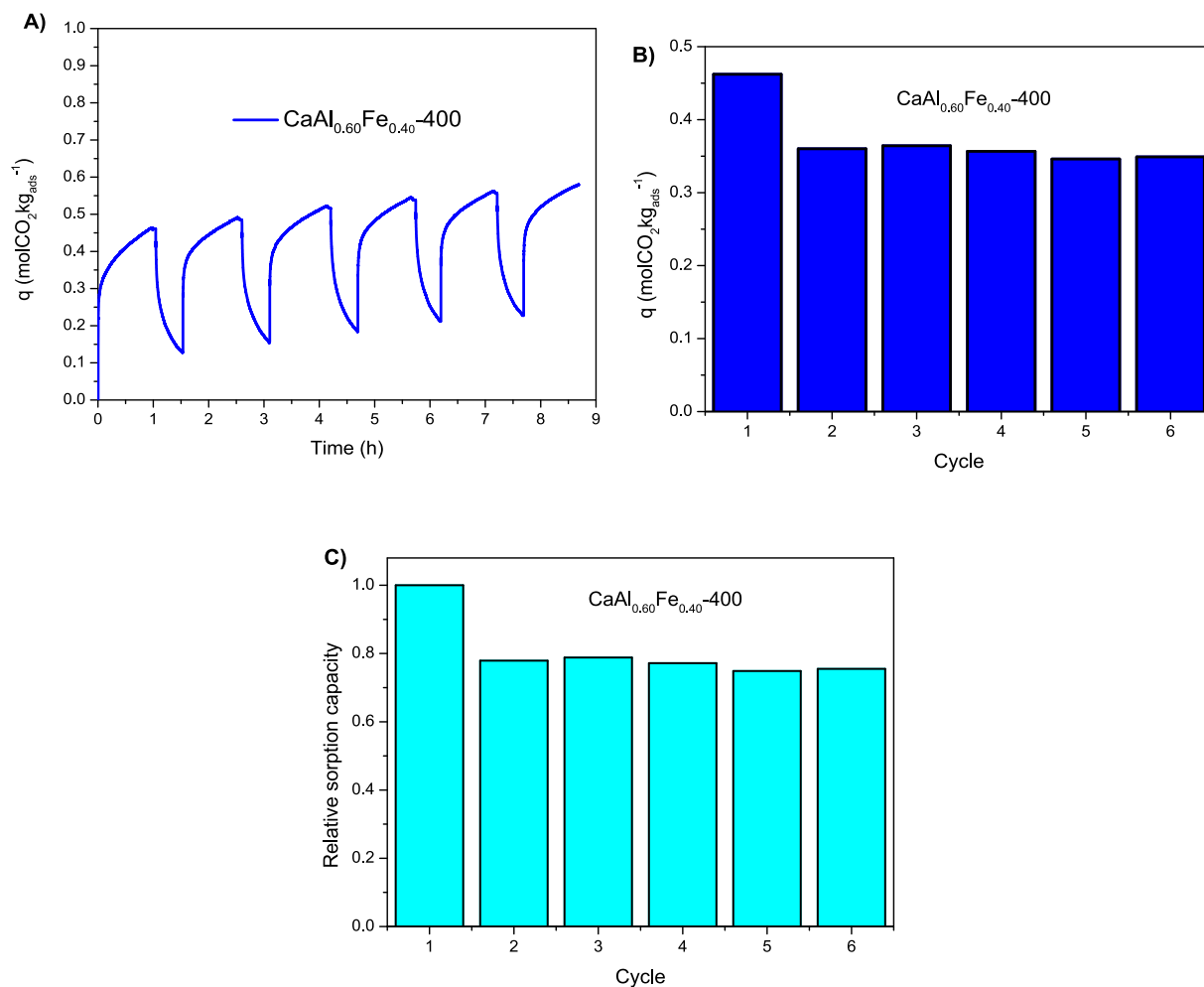
Fig. 6. Sorption–desorption of CO_2 cycles on sample CaAl$_{0.60}$Fe$_{0.40}$–400 under sorption conditions of $p_{CO2} = 0.3$ bar and 300 °C and desorption conditions of vacuum and 300 °C. A: sorption capacity as a function of time. B: sorption capacity of each cycle. C: relative sorption capacity obtained for CaAl$_{0.60}$Fe$_{0.40}$–400 after consecutive sorption–desorption cycles (i.e., sorption capacity normalized by that in the 1st cycle).

behavior in cyclic sorption–desorption processes, which is not the case, as shown herein below.

In order to evaluate the behavior of CaAlFe–MMOs in cyclic CO_2 sorption–desorption processes and taking into account the similar behavior that exists between CaAlFe–LDHs calcined at 400 °C and those calcined at 750 °C, the $CaAl_{0.60}Fe_{0.40}$–400 sample was selected for subsequent static sorption–desorption experiments. Fig. 6A shows the variation of CO_2 sorption capacity as a function of time. The sorption cycles extended along 1 h, while the desorption cycles for 0.5 h. From data in Fig. 6A, a good behavior of this sample in the sorption–desorption cyclic processes could be verified, with fast sorption and desorption kinetics. However, it is also important to consider that, according to the literature [58], the CO_2 desorption rate is lower than the adsorption rate. For this reason, more CO_2 was adsorbed than desorbed in the first cycle, i.e., an increasing fraction of CO_2 remained adsorbed on the sorbent (see the starting point of each cycle in Fig. 6A). This implied a decrease in the sorption capacity and both sorption and desorption values tended to the value of the cyclic work capacity as the cyclic process was carried out, which agreed with the mechanism proposed in this work.

The highest q value was observed in the first cycle, and the desorption process did not completely remove all adsorbed CO_2. In other words, after the first sorption cycle a fraction of CO_2 had been irreversibly adsorbed. Assuming the mechanism above described, two forms of CO_2 sorption, one through CaO and another through $Ca_2Fe_2O_5$, it could be tentatively concluded that the irreversibly adsorbed fraction would take place on CaO to form $CaCO_3$, which would not decompose under the desorption conditions (vacuum and 300 °C). However, according to the literature [18], the possible presence of Cl^- (since this is not removed by calcination at 400 °C [3,52]) could promote the decomposition of $CaCO_3$ at lower temperatures than in the absence of chloride. The reversible sorption of CO_2 would take place on $Ca_2Fe_2O_5$ to form $CaCO_3$ and Fe_2O_3.

According to data in Fig. 6B and 6C, the capacity remained constant between the second and the sixth cycle, which is almost 80% of that exhibited in the 1st cycle (Fig. 6C). Despite the formation of $CaCO_3$ (see section 3.4), it can be concluded that the sample $CaAl_{0.60}Fe_{0.40}$–400 displayed a suitable behavior to be used in cyclic sorption–desorption processes.

3.3.2. Dynamic experiments

Based on the results obtained in the static experiments, the CaAl–400, $CaAl_{0.60}Fe_{0.40}$–400 and CaFe–400 samples were selected for the dynamic studies; these samples correspond to those without iron,

with all aluminum replaced by iron, and the best CO_2 sorbent. The capture capacity, stability and regeneration of the materials are essential parameters for their application as CO_2 adsorbents on an industrial scale for pre–combustion and post–combustion applications. In order to determine the working capacity, the selected samples were submitted to successive CO_2 sorption–desorption cycles at 400 °C and a CO_2 partial pressure of 0.15 bar (total pressure of 1 bar). After being submitted to a 5–cycle sorption–desorption process under the conditions described above, used $CaAl_{0.60}Fe_{0.40}$–400 sample was submitted to a 5–cycle sorption–desorption process in the presence of water vapor during the sorption steps (15 vol% CO_2 and 15 vol% H_2O balanced with N_2); this is relevant as steam is often present in such type of streams. After this cyclic process in the presence of water vapor, the same sample was again submitted to 5 sorption–desorption cycles in the absence of water. The desorption cycles were carried out in a N_2 stream (100 mL/min) at 400 °C and 1 bar pressure. The breakthrough curves are shown in Fig. S9.

The CO_2 sorption capacities of samples CaAl–400, $CaAl_{0.60}Fe_{0.40}$–400 and CaFe–400 calculated from Eq. (2) are shown in Fig. 7A. The highest values of q_d for each sample were determined for the first cycle, in agreement with literature data for other MMOs derived from LDHs [17,50,58,66]. It is noteworthy that the sample that presented the highest q_d value in each cycle was always $CaAl_{0.60}Fe_{0.40}$–400 (q_d (first cycle) = 1.22 $mol_{CO2} \cdot kg_{ads}^{-1}$), followed by sample CaFe–400 (q_d (first cycle) = 1.10 $mol_{CO2} \cdot kg_{ads}^{-1}$) and finally sample CaAl–400 (q_d (first cycle) = 0.79 $mol_{CO2} \cdot kg_{ads}^{-1}$), in agreement with the trends observed in the static tests (Figs. 4 and 5). After the first cycle there was a loss of sorption capacity and afterwards it remained practically constant. Fig. 7B shows the sorption capacity relative to the first cycle of each sample. The sample with the highest loss of capacity after the first cycle was CaFe–400 (close to 25 % of its maximum q), followed by $CaAl_{0.60}Fe_{0.40}$–400. Finally, CaAl–400 sample had the lowest capacity loss after one cycle. After 5 cycles, all samples maintained a sorption capacity of approximately 63% of that of the first cycle, which confirmed the usefulness of CaAlFe–MMOs as potentially suitable materials in CO_2 capture.

According to the literature [17,58,67], CO_2 adsorbents formed by calcination of LDHs present an improvement of the CO_2 sorption capacity in the presence of steam in the fed gas stream. To evaluate the influence of the presence of water during CO_2 sorption on CaAlFe–MMOs, the most promising $CaAl_{0.60}Fe_{0.40}$–400 sample was submitted to 5 sorption–desorption cycles in dry conditions, then to cycles 5 in the presence of water vapor and, after that, to another 5 cycles in the absence of water vapor. Fig. 8A shows the CO_2 sorption capacities of the
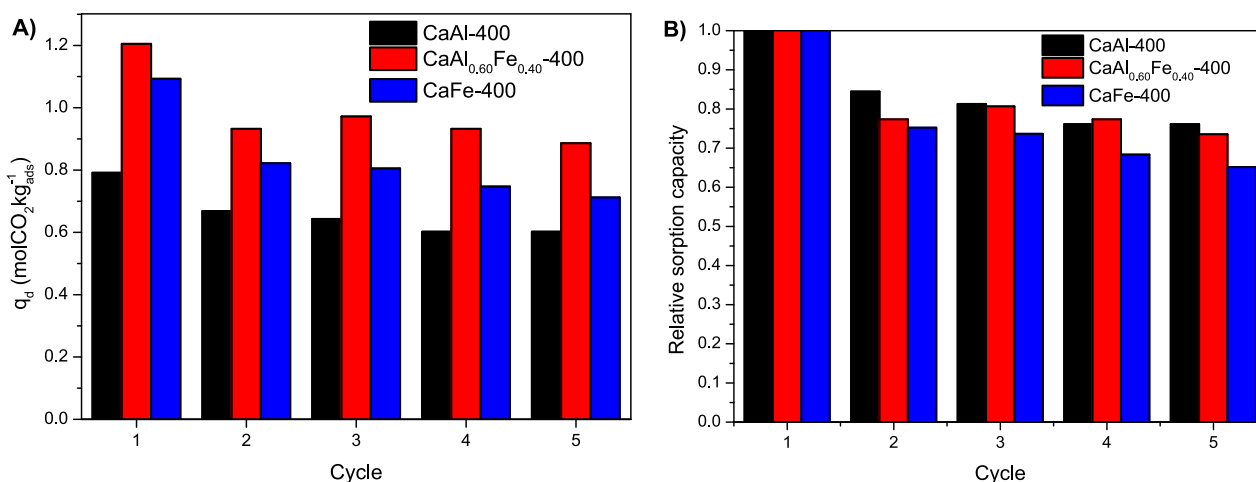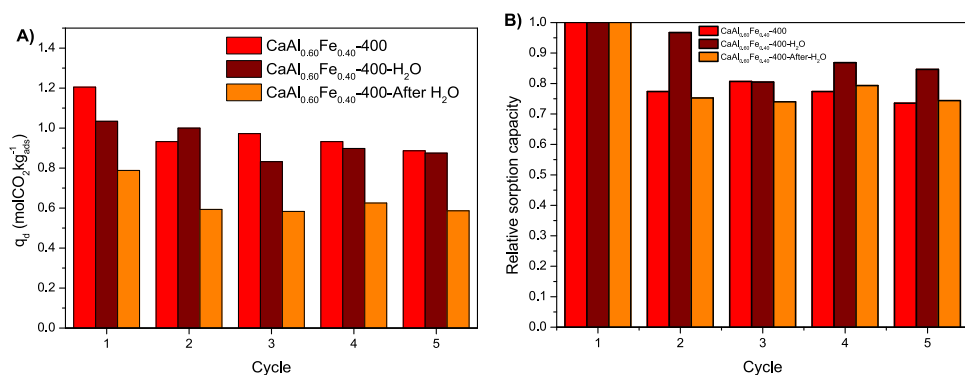

Fig. 7. A) CO_2 sorption capacity and B) relative sorption capacity obtained for CaAl–400, $CaAl_{0.60}Fe_{0.40}$–400 and CaFe–400 after consecutive sorption–desorption cycles. Sorption conditions: T = 400 °C, p_{CO2} = 0.15 bar (P_T = 1 bar), total flow rate = 100 mL/min and feed composition = 15 vol% of CO_2 balanced with N_2. Desorption conditions: T = 400 °C, P_T = 1 bar and 100 mL/min of pure N_2.

Fig. 8. A) CO_2 sorption capacity and B) relative sorption capacity for samples $CaAl_{0.60}Fe_{0.40}-400$, $CaAl_{0.60}Fe_{0.40}-400-H_2O$ and $CaAl_{0.60}Fe_{0.40}-400-After-H_2O$ after consecutive sorption–desorption cycles. Sorption conditions: T = 400 °C, p_{CO2} = 0.15 bar (P_T = 1 bar), total flow rate = 100 mL/min and feed composition = 15 vol% of CO_2 balanced with N_2. In experiments with water vapor feed composition = 15 vol% of CO_2 and 15 vol% of H_2O balanced with N_2 and P_T = 1 bar. Desorption conditions: T = 400 °C, P_T = 1 bar and 100 mL/min of pure N_2.

$CaAl_{0.60}Fe_{0.40}-400$ sample in the absence of water, in the presence of water and again in the absence of water. All experiments were performed consecutively on the same sample. When CO_2 sorption was performed in the presence of water vapor, the sample capacity reached a value of 1.03 $mol_{CO2} \cdot kg_{ads}^{-1}$ in the first cycle (85% of the capacity in dry cycle 1). However, in the last cycle in the absence of water vapor, sample $CaAl_{0.60}Fe_{0.40}-400$ showed a relative capacity of 74%, so the presence of steam in the feed was favorable for CO_2 sorption. In the last cycle in the presence of steam, the capacity was 85% of the maximum capacity in the presence of water vapor, a value similar to that observed in the absence of water vapor. After the 5 cycles performed in the presence of water vapor, the sample was again submitted to another 5 cycles in dry conditions. In this case, the capacity of the first cycle was 0.79 $mol_{CO2} \cdot kg_{ads}^{-1}$, which was 75% of the first cycle performed under dry conditions. Fig. 8B shows how the presence of water decreased the relative loss of sorption capacity as the number of cycles increased until 5th cycle, while in the absence of water the loss of sorption capacity between cycles was greater than in the presence of water vapor. Therefore, the presence of water vapor had a favorable effect on CO_2 sorption on CaAlFe–MMOs materials.

Finally, Table 2 summarizes the CO_2 sorption capacities of the CaAlFe–MMOs determined in both static and dynamic experiments. It is worth mentioning that, for the same material under the same conditions, CO_2 sorption capacities determined from both methods were similar (difference below 10% - data not shown for brevity).

All samples evaluated in CO_2 sorption, except $CaAl_{0.80}Fe_{0.20}$, presented CO_2 capture capacities higher than the limiting value (0.30 $mol_{CO2} \cdot kg_{ads}^{-1}$ [19,20]) established for a material to be used as a CO_2 adsorbent in pre–combustion processes. The CaAl–400 sample showed a increase of q when passing from the experiments performed in static to the experiments performed in dynamic conditions, the value of q_d being

1.5 times the value of q_e. Considering the phase composition of sample CaAl–400 and the proposed mechanism through sorption on CaO, larger values for q_d than for q_e would be expected, since according to literature [3,5,6], CO_2 sorption on CaO–based materials has its optimal operating range between 500 °C and 800 °C. The increase in q for CaAl–400 sample when switching from static to dynamic experiments would be justified by the increase in temperature that favors the endothermic effects of sorption and by the mechanism of sorption through CaO that was favored at high temperatures [3,5,6]. In the CaFe–400 sample, in which the sorption mechanism seemed to be through sorption on the $Ca_2Fe_2O_5$ phase, an increase in q was also observed when going from static to dynamic experiments. This increase could be justified by increasing the sorption temperature from 300 °C to 400 °C, since, according to Gupta et al. [65], there is a rapid increase in the amount of CO_2 adsorbed in the range near 400 °C up to 600 °C. Therefore, increasing the temperature favored sorption on the $Ca_2Fe_2O_5$ phase. The slight decrease observed in the $CaAl_{0.60}Fe_{0.40}-400$ sample observed when switching from static to dynamic experiments could be attributed to the decrease in p_{CO2} from 0.3 bar to 0.15 bar.

As indicated above, CO_2 sorption on CaAlFe–MMOs ternary has hardly been studied. Narayanappa and Vishnu–Kamath [18] studied CO_2 sorption on CaAl–MMOs and on CaFe–MMOs in the temperature range 350–550 °C, finding that the solid containing Fe^{3+} presented a sorption capacity of 1.9 $mol_{CO2} \cdot kg_{ads}^{-1}$ being twice higher than that of the CaAl–MMOs sample of the same work and at the same time it also presents a higher value than that reported in this work for CaFe–LDH calcined both at 400 °C and 750 °C. However, it is important to take into account that in the present work the experiments were carried out at a lower temperature (300 °C). On the other hand, the sorption capacities for MgAl–MMOs are presented in Table 3. In some cases, part of the aluminum has been replaced by Ga^{3+} and/or doped with K^+ and/or Na^+, which has a positive effect on the sorption capacity [50,58,67]. In general terms, it is observed that the samples tested in this work present higher sorption capacities than the MgAl–MMOs and similar to the MgAl–MMOs enhanced with K^+, Na^+ or Ga^{3+} doping; being for all cases the sorption temperature of 300 °C, while the p_{CO2} varies between 0.3 and 1.00 bar.

3.4. Characterization of the used solids

To verify the sorption mechanism proposed in section 3.2, samples used in CO_2 capture were characterized by PXRD, FT–IR, thermal analysis and electron microscopy. The FT–IR spectra of the samples used in the dynamic experiments are not included due to their similarities with those used in the static experiments.

3.4.1. Solid used in the static experiments
Fig. S10A shows the powder X–ray patterns of the samples calcined at 400 °C after being used in CO_2 sorption (static experiments). The diffractograms of the samples were like those shown in Fig. 1A for the

Table 2
CO_2 sorption capacities of samples in static and dynamic experiments.

Sample	CO_2 sorption capacity ($mol_{CO2} \cdot kg_{ads}^{-1}$)		
	q_e, Static experiments (conditions: p_{CO2} = 0.3 bar, T = 300 °C)		q_d, Dynamic experiments (conditions: p_{CO2} = 0.15 bar, P_T = 1 bar, T = 400 °C, feed = 100 mL/min balanced with N_2)
	Calcined at 400 °C	Calcined at 750 °C	Calcined at 400 °C
CaAl	0.52	0.47	0.79
$CaAl_{0.80}Fe_{0.20}$	0.23	0.27	*
$CaAl_{0.60}Fe_{0.40}$	1.55	1.56	1.22
$CaAl_{0.40}Fe_{0.60}$	1.02	*	*
$CaAl_{0.20}Fe_{0.80}$	1.01	*	*
CaFe	0.84	0.84	1.10
$CaAl_{0.60}Fe_{0.40}-H_2O$	*	*	1.03
$CaAl_{0.60}Fe_{0.40}-after-H_2O$	*	*	0.79

*Not determined.

Table 3

CO_2 sorption capacities of samples in static and dynamic experiments.

CO_2 Sorbent	Sorption Capacity ($mol_{CO2} \cdot kg_{ads}^{-1}$)	Temperature (°C)	p_{CO2} (bar)	Reference
8.5HT7	1.62	300	1.00	[17]
8.5HT15	1.11	300	1.00	[17]
8.5HT10	1.07	300	1.00	[17]
HTC–CO_3	1.05	300	1.00	[50]
HTC–CO_3(Ga)	1.15	300	1.00	[50]
HTC–CO_3_K	1.43	300	1.00	[50]
HTC–CO_3(Ga)_K	1.45	300	1.00	[50]
HTC–10 Ga–20 K	1.82	300	1.08	[20]
cK–HTCGa MW	1.70	300	1.05	[20]
MG61–K_2CO_3	1.31	300	0.34	[62]
HTI–K–Na	1.10*	300	0.40	[67]
CaAl–400	0.52	300	0.30	This work
CaAl–750	0.47	300	0.30	This work
$CaAl_{0.80}Fe_{0.20}$–400	0.23	300	0.30	This work
$CaAl_{0.80}Fe_{0.20}$–750	0.27	300	0.30	This work
$CaAl_{0.60}Fe_{0.40}$–400	1.55	300	0.30	This work
$CaAl_{0.60}Fe_{0.40}$–750	1.56	300	0.30	This work
CaFe–400	0.84	300	0.30	This work
CaFe–750	0.84	300	0.30	This work

*Under wet conditions.

fresh samples; the main difference was the appearance of the diffraction peaks corresponding to the $CaCO_3$ phase. In all samples, the diffraction peak at a 2θ value of 29.4° characteristic of $CaCO_3$ was observed (ICDD 01–072–1937). This confirmed that CO_2 sorption on CaAlFe–MMOs took place through a sorption mechanism involving the formation of $CaCO_3$, although depending on the presence and relative amount of Fe^{3+} this took place by reaction of CO_2 with CaO (samples with low Fe^{3+} content) or with $Ca_2Fe_2O_5$ (samples with high Fe^{3+} content). In all samples (except $CaAl_{0.60}Fe_{0.40}$–400–used), an halo was observed in the 2 θ range from 15° to 35°, characteristic of the presence of amorphous mixed oxides [25]. In sample $CaAl_{0.60}Fe_{0.40}$–400–used this hump was not observed due to the high crystallinity of the $CaCO_3$ formed. No additional crystalline phases were identified.

Fig. S10B shows the powder X–ray patterns of the samples calcined at 750 °C used in the CO_2 capture (static experiments). The diffractograms in Fig. S10B are identical to those shown in Fig. 1B, the main difference was, once again, the presence of the diffraction peak at 29.4° (2 θ) characteristic of $CaCO_3$. This peak at 29.4° can also be identified in Fig. 1B for sample $CaAl_{0.60}Fe_{0.40}$–750, although its intensity was quite lower than in the diffractogram of the same sample after being used in CO_2 capture; it may be due to the high capacity of this sample to capture CO_2, in this case atmospheric CO_2, during handling. According to the mechanism proposed, CO_2 capture in CaFe–750 sample would take place through the $Ca_2Fe_2O_5$ phase to produce $CaCO_3$ and Fe_2O_3, since CaO had not been identified in Fig. 1B, i. e., prior to the capture experiments. After sorption, the presence of $CaCO_3$ was observed by PXRD, but Fe_2O_3 was not detected. This could occur because the temperature at which CO_2 capture was performed (300 °C for the static tests) was not high enough for crystallization of Fe_2O_3. When CaFe–LDH was calcined for 2 h at 400 °C, the presence of an amorphous material and broad and not very intense diffraction peaks corresponding to Fe_2O_3 were observed (Fig. 1). On the other hand, the high crystallinity of the other phases in the CaFe–750-used sample could mask the presence of the weak diffraction peaks of the Fe_2O_3 formed. The absence of CaO in the CaFe–750 sample and the formation of $CaCO_3$ in the CaFe–750-used sample agreed with the CO_2 capture mechanism proposed for CaAlFe–MMOs.

Fig. S11A and S11B show the FT–IR spectra of the samples calcined at 400 °C and 750 °C used in CO_2 capture (static experiments), respectively. The shapes of the spectra were similar to those shown in Fig. S3A and S3B. A broad band was recorded in the 3700–3400 cm^{-1} range, due to the overlapping of the bands of the stretching vibrations of the hydroxyl groups under different environments [15,18,19,37]. The band at 1637 cm^{-1} confirmed the presence of water molecules, while the bands

at 1427 and 874 cm^{-1} confirmed the presence of $CaCO_3$ formed after CO_2 sorption [15,18,19,37]. The bands due to M—OH bonds, where M can be Ca^{2+}, Al^{3+} or Fe^{3+}, were recorded in the 700 to 400 cm^{-1} range [19]. These results agreed with those observed by PXRD.

Fig. 9A and 9B show two SEM micrographs of the CaAl–400–used sample. The aggregates of smooth particles with hexagonal shape have disappeared, being observed aggregates of size between 50 and 60 μm which in turn were made up of smaller particles with rounded shape, giving the aggregate a flaky and spongy appearance. SEM micrographs of $CaAl_{0.60}Fe_{0.40}$–400–used sample are shown in Fig. 9C and 9D. Here again, differences are observed with respect to the same sample before being used in CO_2 sorption. After use, aggregates of particles of approximately 5 μm in size were observed. These aggregates appeared to be coated or enveloped by plate–shaped particles of irregular morphology. The presence of these plate–like particles could be attributed to the fact that at 400 °C the layered structure does not disappear completely [25]. The detection of the layered structure by PXRD could be expected; however, the cyclic experiments were performed at 400 °C and at this temperature the layered structure was destroyed and not detected by PXRD (Fig. S10A), although SEM micrographs showed the presence of hexagonal sheet–like particles characteristic of LDH–type compounds [24,25,47]. Finally, Fig. 9E and 9F show SEM micrographs of the CaFe–400–used sample. In this case, the appearance, morphology and size of the particle aggregates and particles were similar to those described for the fresh CaFe–400 sample [25].

Fig. 10A and 10B show two SEM micrographs of the CaAl–750–used sample. The morphology and appearance of the particle aggregates have changed radically. After being used, the plate–like particle aggregates were no longer observed, but rather particles with a rough appearance, growing on top of each other and having a higher degree of sintering and a less porous surface. SEM micrographs of the $CaAl_{0.60}Fe_{0.40}$–750–used sample are shown in Fig. 10C and 10D. In the case of this sample, some changes in the morphology and appearance of the particle aggregates were also observed after being used in CO_2 capture, resulting in larger particle aggregates, higher degree of sintering and a less rough and flaky surface. In addition, the irregular plate–shaped particles that were observed for the fresh sample have disappeared. Finally, Fig. 10E and 10F show the SEM micrographs of the CaFe–750 sample. In this sample, hardly any changes in the morphology and appearance of the particle aggregates were observed, the main difference was a slight loss of roughness and sponginess of the particle aggregates.

Fig. 11A shows the thermal behavior of sample $CaAl_{0.60}Fe_{0.40}$–400 after being subjected to 6 CO_2 sorption–desorption cycles. According to the TG curve, the total mass loss was 23.06%, which took place through 5 steps in agreement with the concavity changes observed in the DTG curve. The first two steps were overlapping each other, the first one centered at 75 °C and the second one at 160 °C. The first process centered at 75 °C, which involved a mass loss of 1.76%, could be attributed to the loss of water absorbed on the surface of the solid [26], although water was not detected by EGA, and concluded at 130 °C. According to the literature [25,26,52], the sequence of thermal decomposition of hydrocalumite–type compounds is: removal of physisorbed water, dehydration, dehydroxylation and decarbonylation or loss of the last hydroxyl groups. As it can be seen in the SEM micrographs (Fig. 2C and 2D and Fig. S5G–I), the hexagonal plate-shaped particles characteristic of LDHs were not destroyed at 400 °C, so it could be concluded that the first two mass losses corresponded to physisorbed water removal and dehydration. On the other hand, according to the EGA analysis, the mass losses corresponding to the DTG peaks centered at 354, 565 and 653 °C corresponded to the elimination of CO_2. The third step began at 276 °C and concluded at 431 °C, while the fourth step began at 481 °C and concluded at 598 °C. The fifth step, which started at 598 °C and ended at 684 °C, can be attributed to the decomposition of $CaCO_3$. These data justify the good behavior of this sample in the cyclic processes shown in Fig. 6. In the first sorption cycle, the capture capacity was higher than in the other cycles, since there was an amount of CO_2
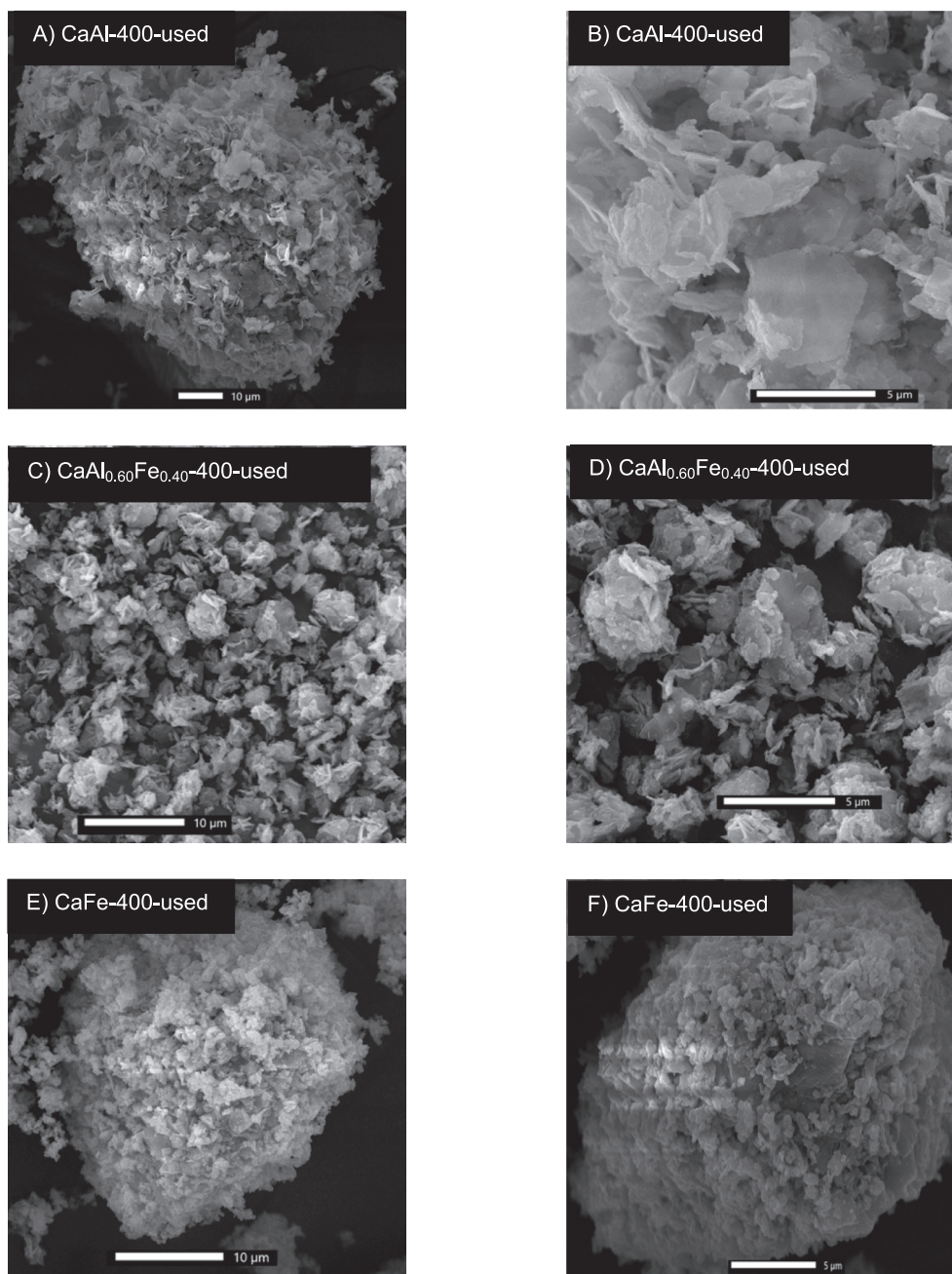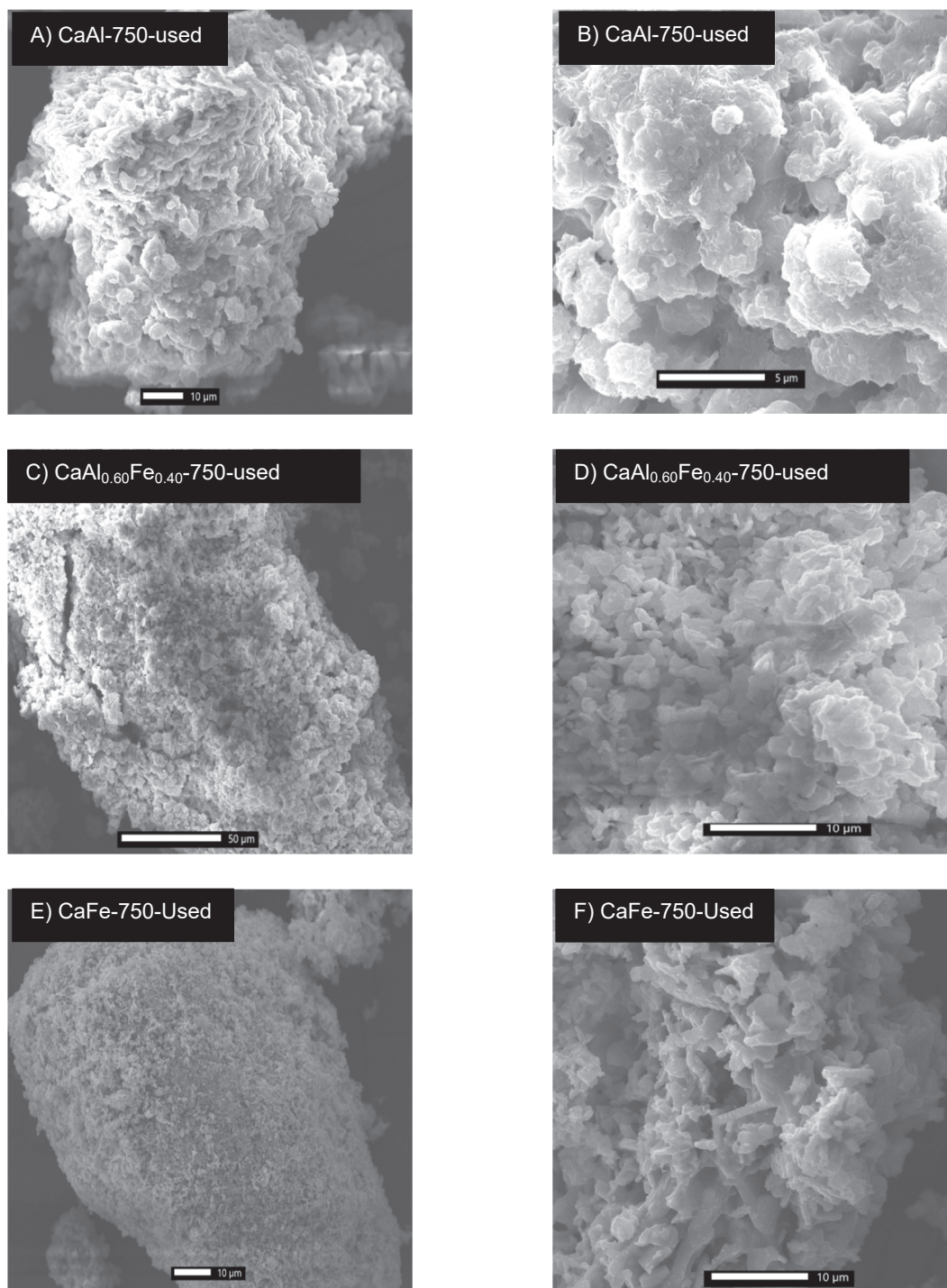
Fig. 9. SEM micrographs of samples calcined at 400 °C after being used in CO_2 sorption. Fig. A and B: CaAl–400–used sample. Fig C and D: $CaAl_{0.60}Fe_{0.40}$–400–used sample. Fig E and F: CaFe–400–used sample.

that was strongly adsorbed, forming $CaCO_3$, which in the conditions in which the adsorbent was regenerated (vacuum and 300 °C) did not decompose (irreversible sorption). Fig. 11B shows the presence of three different types of basic centers [17]: weak (354 °C), medium (565 °C) and strong (653 °C).

3.4.2. Solid used in dynamic experiments

The PXRD patterns of the solids used in the dynamic experiments, as well as the diffractograms after being subjected to the regeneration process, are shown in Fig. 12. Fig. 12A shows the diffractograms of sample CaAl–400-used in dynamic conditions, with $CaCO_3$ being the only crystalline phase identified. After the regeneration process, a considerable decrease in the intensity of the $CaCO_3$ phase diffraction peaks was observed. These results agree with the mechanism proposed in this work for CO_2 sorption on samples with no or low Fe^{3+} content,

where the phase responsible for the capture forming $CaCO_3$ is CaO. Fig. 13A and Fig. S12A show the thermal curves and EGA analysis of sample CaAl–400-used in dynamic experiments. The thermal decomposition sequence was like that described for sample $CaAl_{0.60}Fe_{0.40}$–used in static cycles, where the processes of physiosorbed water removal and dehydration could overlap. In this case, four mass loss steps were observed, the first two of them centered at 75 °C (physiosorbed water removal) and 160 °C (dehydration) involving mass loss of 5.93%. Then, the loss steps centered at 400 °C and 685 °C, involving mass loss of 17.17%. According to EGA, the first two processes correspond to H_2O loss and the last two to CO_2 emission. The third step started around 250 °C and overlapped with the fourth step, which started around 470 °C. This justifies the behavior shown in Fig. 7. After the first cycle, the sorption capacity decreased, due to the formation of $CaCO_3$, which did not decompose under the regeneration conditions of the adsorbents

Fig. 10. SEM micrographs of samples calcined at 750 °C after being used in CO_2 sorption. Fig. A and B: CaAl–750–used sample. Fig. C and D: $CaAl_{0.60}Fe_{0.40}$–750–used sample. Fig. E and F: CaFe–750–used sample.

(400 °C and N_2 flow). But there was CO_2 capture on low strength basic centers, which were regenerated under the conditions used. The existence of two different types of basic centers, weak and strong, justifies the good behavior of this sample in cyclic CO_2 sorption processes, as well as the mechanism proposed.

The diffractograms of the CaFe–400 sample after being used in the dynamic experiments and after regeneration are shown in Fig. 12C. After being used in the dynamic CO_2 capture experiments, the phases identified by PXRD were $CaCO_3$ and Fe_2O_3, which agreed with the CO_2 capture mechanism proposed. Moreover, after the regeneration process,

the intensity of the diffraction peaks corresponding to the $CaCO_3$ phase decreased, indicating that CO_2 sorption on CaAlFe–MMOs with high Fe^{3+} content was more easily reversed than on those with low Fe^{3+} content: $CO_2 + Ca_2Fe_2O_5 \rightarrow CaCO_3 + Fe_2O_3$. However, after the regeneration process, $CaCO_3$ was still observed. This remaining calcite could be formed by the reaction between CO_2 and some segregated Ca-phase in the CaFe–400 sample, in which no free CaO and doubtfully CaOHCl were identified. On the other hand, the thermal curves of the CaFe–400-used in dynamic experiments are shown in Fig. 13C and Fig. S12C. From the TG and DTG curves it can be concluded that the
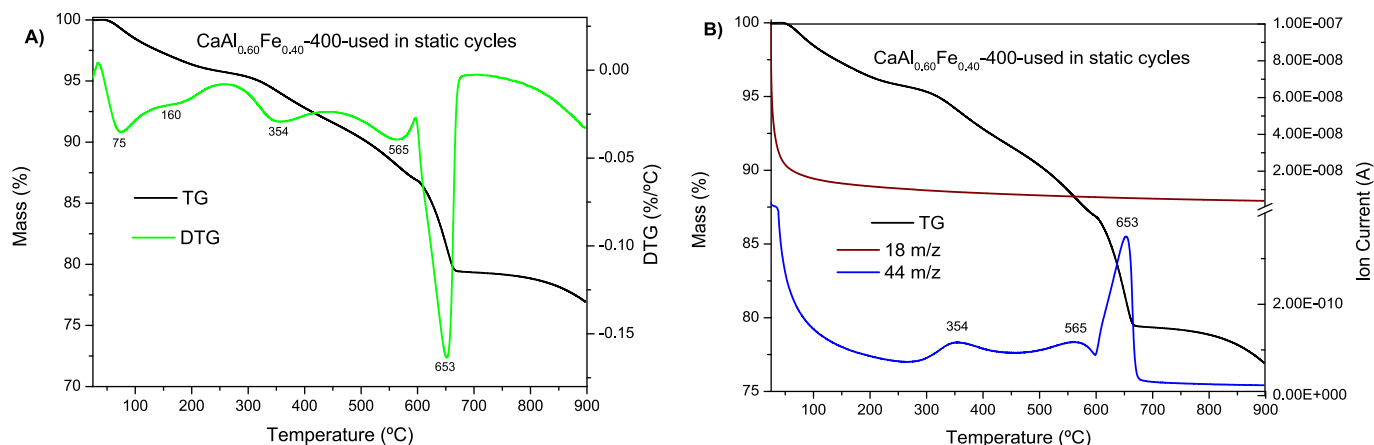
Fig. 11. Thermal curves of $CaAl_{0.60}Fe_{0.40}$–400 after being used in static cycles: TG and DTG curves (A) and TG and EGA curves (B) (18 m/z = water; 44 m/z = CO_2).
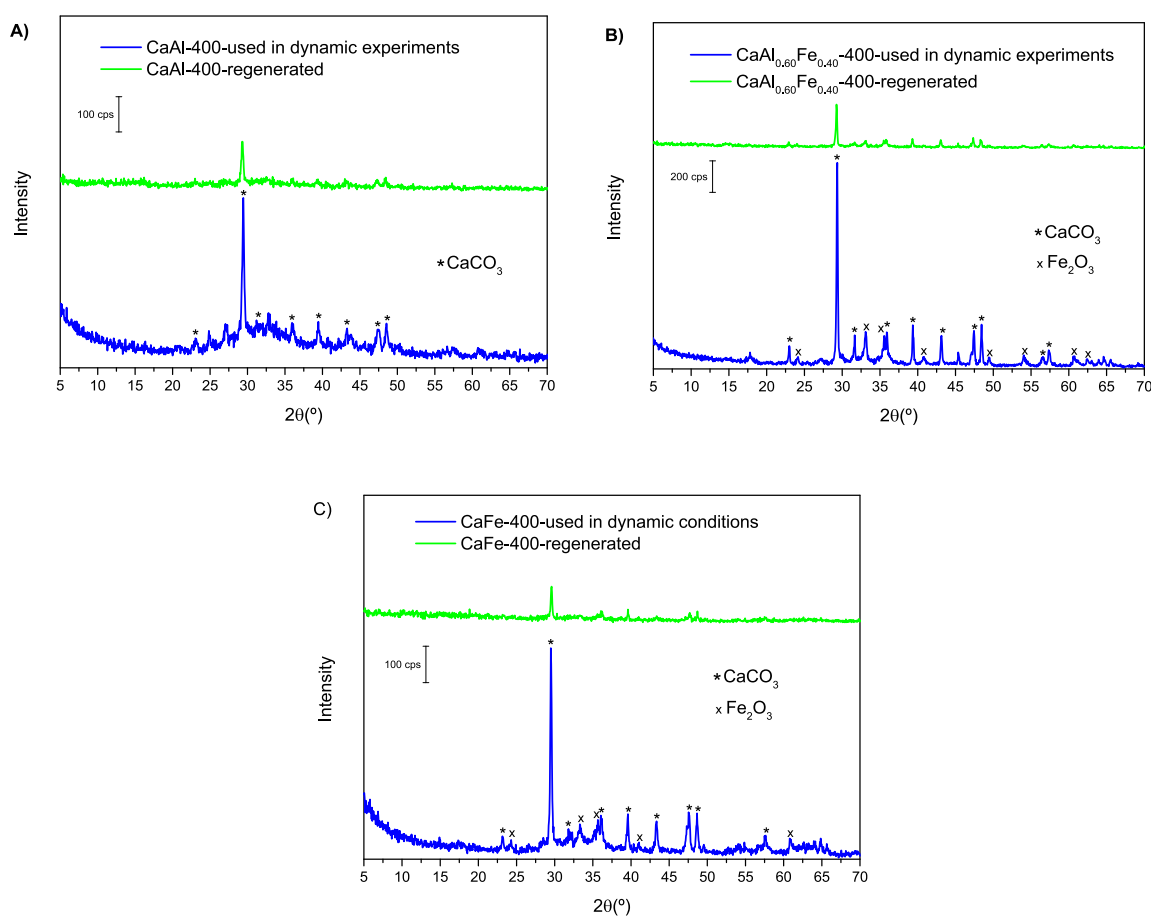

Fig. 12. Powder X–ray patterns of samples after being used in CO_2 sorption and after being regenerated (dynamic experiments). A) CaAl–400 sample, B) $CaAl_{0.60}Fe_{0.40}$–400 sample, and C) CaFe–400 sample.

thermal decomposition of this sample took place through 5 steps with a total mass loss of 32.88%. The first two steps, centered at 63 °C and 98 °C and involving a mass loss of 14.25%, could correspond to the removal of physiosorbed water, according to EGA, while those centered at 295 °C, 545 °C and 620 °C and involving mass losses of 2.61 %, 8.74 % and 7.28 %, respectively, corresponded to CO_2 emission according to the EGA. These results agreed with the PXRD results and with the proposed mechanism. Results in Fig. 13C suggested the presence of three different types of basic centers in the CaFe–400 sample: weak (295 °C), medium (545 °C) and strong (620 °C) [17].

The diffractograms of sample $CaAl_{0.60}Fe_{0.40}$–400 after being used in the dynamic experiments and after being regenerated are shown in Fig. 12B. The phases identified after submitting this sample to the dynamic experiments were the same identified in the CaFe–400 sample, in agreement with the CO_2 sorption mechanism proposed. After the regeneration process, the only phase identified was $CaCO_3$, although the intensity of its diffraction peaks was higher than in the case of the CaFe–400-regenerated sample. On the other hand, the thermal curves of CaFe–400-used in dynamic experiments are shown in Fig. 13B and Fig. S12B. From the TG and DTG curves it can be concluded that the
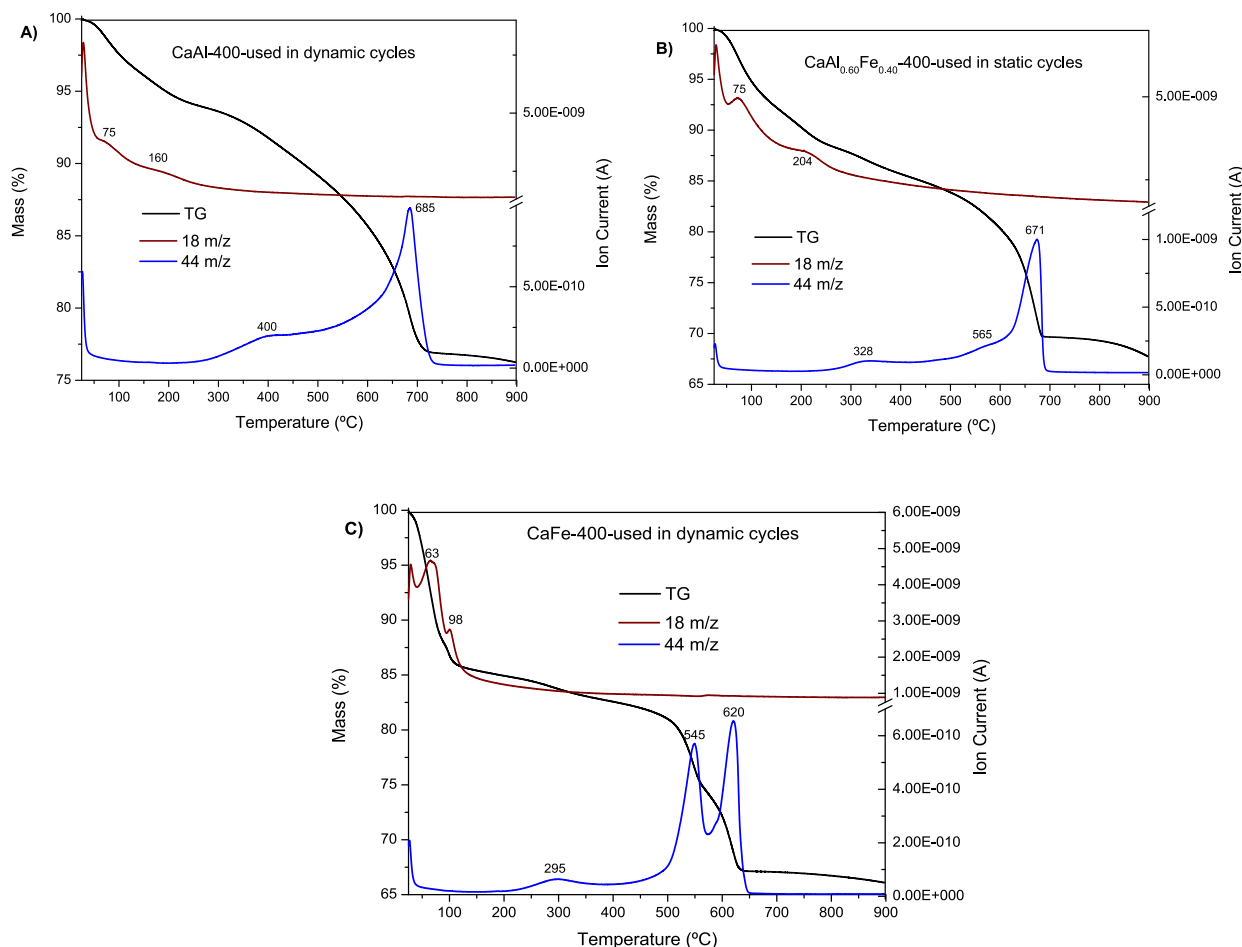
Fig. 13. TG and EGA curves of samples after being used in CO_2 in dynamic experiments. A) CaAl–400 sample, B) CaAl$_{0.60}$Fe$_{0.40}$–400 sample, and C) CaFe–400 sample.

thermal decomposition of this sample took place through 5 steps with a total mass loss of 32.24%, although the degree of overlapping between the processes, especially between the first and second ones and between the fourth and fifth ones, was much greater than in the case of the CaFe sample. According to the EGA results, the first two processes centered at 75 °C and 204 °C and involving mass losses of 7.11 % and 4.58 %, corresponded to the removal of H_2O, while the third process centered at 328 °C with a mass loss of 2.47 %, the fourth process centered at 565 °C and overlapped with the fifth one centered at 671 °C with a mass loss of 16.19 %, corresponded to CO_2 emission. These results suggested the presence of three types of basic centers: weak (328 °C), medium (565 °C) and strong (671 °C) [17].

Table 4 shows the basic center types of each of the samples used in the dynamic experiments, based on the EGA results obtained. All the samples showed weak, medium and strong basic centers, except CaAl–400, where it was not possible to discriminate between medium and strong strength centers due to the overlapping of the processes. The incorporation of Fe^{3+} implied a decrease in the temperature at which CO_2 was removed. In the case of the weak basic centers, increasing the

Fe^{3+} content up to 40 % of the trivalent metal, the temperature at which CO_2 was removed decreased by 72 °C, while going to 100 % Fe^{3+} decreased it by another 33 °C. This same behavior was observed for the basic centers of average strength between the CaAl$_{0.60}$Fe$_{0.40}$–400 and CaFe–400 samples with a temperature decrease of 20 °C. In the case of the strong basic centers, increasing the Fe^{3+} content to 40 % decreased the temperature by 14 °C, and increasing it to 100 % decreased it by another 51 °C. Considering these results, it could be concluded that the presence of Fe^{3+} produced a decrease in the strength of the basic centers.

4. Conclusions

Potentially suitable materials for application as CO_2 adsorbents were prepared by calcination of hydrocalumite–like CaAlFe–LDHs at 400 °C and 750 °C, which have been prepared from a waste–salt cake. The isomorphic substitution of Al^{3+} for Fe^{3+} in the starting LDH played a fundamental role in the different phases formed in the calcination products (MMOs) of LDHs. In the case of samples calcined at 400 °C, a mixture of amorphous mixed oxides was obtained, whereas when calcined at 750 °C, highly crystalline products were obtained. When there was no Fe^{3+} in the starting LDH, the phases formed at 750 °C were mayenite, CaClOH and CaO. As the Fe^{3+} content increased (from $m = 0$ to $m = 0.2$), Ca$_2$FeO$_3$Cl was additionally identified. When m increased from 0.2 to 0.4, in addition to the phases mentioned so far, Ca$_2$Fe$_2$O$_5$ was also formed. When Al^{3+} was completely replaced by Fe^{3+}, only Ca$_2$Fe$_2$O$_5$, Ca$_2$FeO$_3$Cl and CaClOH phases were detected. The presence of the different phases played a fundamental role in CO_2 capture by the derived CaAlFe–MMOs.

Table 4
Types of basic center in the samples [17].

Sample	Temperature of removal of CO_2 (°C)		
	Weak	Medium	Strong
CaAl–400	400	–	685
CaAl$_{0.60}$Fe$_{0.40}$–400	328	565	671
CaFe–400	295	545	620

From the CO_2 capture experiments performed in static conditions, it was concluded that the sorption mechanism can run through two pathways:

(i) Low Fe^{3+} content samples: the main phase responsible for sorption was CaO dispersed on inert supports, leading to the formation of $CaCO_3$.

(ii) High Fe^{3+} content samples: The main phase responsible for sorption seemed to be $Ca_2Fe_2O_5$, through the reversible reaction:
$Ca_2Fe_2O_5(s) + 2CO_2(g) \rightleftharpoons 2CaCO_3(s) + Fe_2O_3(s)$.

When $m = 0.4$, a synergistic effect seemed to take place, reaching the highest CO_2 capture capacity. The S_{BET} of the samples did not have a great influence on the CO_2 capture process by CaAlFe–MMOs, since upon calcining at 750 °C a decrease in S_{BET} occurred, while the capture capacity (q_e) remained practically constant. The $CaAl_{0.60}Fe_{0.40}$–400 sample showed a good behavior when submitted to cyclic sorption–desorption processes. After the first cycle, the sorption capacity decreased, but subsequently remained constant from the second cycle on.

The dynamic experiments allowed to determine the CO_2 working capacity of samples CaAl–400, $CaAl_{0.60}Fe_{0.40}$–400 and CaFe–400, all of them showing a good behavior despite the formation of $CaCO_3$, whose decomposition could be favored by the presence of chloride species. In addition, the presence of steam in the feed had a positive effect on CO_2 capture by CaAlFe–MMOs materials, which is an important figure for several applications like pre–combustion and post–combustion.

In conclusion, the potential use of CaAlFe–MMOs as CO_2 sorbents is suggested in a cyclic continuous operation for moderate temperature CO_2 capture processes due to high sorption capacity and good cyclic behavior.

Declaration of Competing Interest

The authors declare that they have no known competing financial interests or personal relationships that could have appeared to influence the work reported in this paper.

Data availability

No data was used for the research described in the article.

Acknowledgements

Appendix A. Supplementary data

Supplementary data to this article can be found online at https://doi.org/10.1016/j.cej.2023.145165.

References

[1] D.Y.C. Leung, G. Caramanna, M.M. Maroto-Valer, An overview of current status of carbon dioxide capture and storage technologies, Renew. Sustain. Energy Rev. 39 (2014) 426–443, https://doi.org/10.1016/j.rser.2014.07.093.

[2] Climate action. https://climate.ec.europa.eu/eu-action/international-action-climate-change/climate-negotiations/paris-agreement_es, (2015). (Accessed on 15 January 2023).

[3] Z.H. Hashim, Y. Kuwahara, CO_2 Adsorption on a $CaO–Ca_{12}Al_{14}O_{33}$ composite synthesized from a blast furnace slag and its regenerative ability, ISIJ Int. 63 (2023) 190–196, https://doi.org/10.2355/isijinternational.ISIJINT-2022-310.

[4] A. Al-Mamoori, H. Thakkar, X. Li, A.A. Rownaghi, F. Rezaei, Development of potassium– and sodium-promoted CaO adsorbents for CO2 capture at high temperatures, Ind. Eng. Chem. Res. 56 (29) (2017) 8292–8300.

[5] C.S. Martavaltzi, A.A. Lemonidou, Parametric study of the $CaO–Ca_{12}Al_{14}O_{33}$ synthesis with respect to high CO_2 sorption capacity and stability on multicycle operation, Ind. Eng. Chem. Res. 47 (2008) 9537–9543, https://doi.org/10.1021/ie800882d.

[6] L.K.G. Bhatta, S. Subramanyam, M.D. Chengala, S. Olivera, K. Venkatesh, Progress in hydrotalcite like compounds and metal–based oxides for CO_2 capture: a review, J. Clean. Prod. 103 (2015) 171–196, https://doi.org/10.1016/j.jclepro.2014.12.059.

[7] H. Chen, W. Wang, J. Ding, X. Wei, J. Lu, CO_2 Adsorption capacity of FAU zeolites in presence of H_2O: a monte carlo simulation study, Energy Procedia 105 (2017) 4370–4376, https://doi.org/10.1016/j.egypro.2017.03.929.

[8] E. Khoramzadeh, M. Mofarahi, C. Lee, Equilibrium adsorption study of CO_2 and N_2 on synthesized zeolites 13X, 4A, 5A and beta, J. Chem. Eng. Data 64 (2019) 5648–5664, https://doi.org/10.1021/acs.jced.9b00690.

[9] C. Megías-Sayago, R. Bingre, L. Huang, G. Lutzweiler, Q. Wang, B. Louis, CO_2 adsorption capacities in zeolites and layered double hydroxide materials, Front. Chem. 7 (2019) 1–10, https://doi.org/10.3389/fchem.2019.00551.

[10] A. Iwan, H. Stephenson, W.C. Ketchie, A.A. Lapkin, High temperature sequestration of CO_2 using lithium zirconates, Chem. Eng. J. 146 (2009) 249–258, https://doi.org/10.1016/j.cej.2008.06.006.

[11] M. Seggiani, M. Puccini, S. Vitolo, Alkali promoted lithium orthosilicate for CO_2 capture at high temperature and low concentration, Int. J. Greenh. Gas Control 17 (2013) 25–31, https://doi.org/10.1016/j.ijggc.2013.04.009.

[12] A. Sanna, S. Thompson, K.J. Whitty, M.M. Maroto-Valer, Fly ash derived lithium silicate for in–situ pre–combustion CO_2 Capture, Energy Procedia 114 (2017) 2401–2404, https://doi.org/10.1016/j.egypro.2017.03.1386.

[13] D. Peltzer, J. Mùnera, L. Cornaglia, M. Strumendo, Characterization of potassium doped Li_2ZrO_3 based CO_2 sorbents: Stability properties and CO_2 desorption kinetics, Chem. Eng. J. 336 (2018) 1–11, https://doi.org/10.1016/j.cej.2017.10.177.

[14] M. Seggiani, E. Stefanelli, M. Puccini, S. Vitolo, CO_2 sorption/desorption performance study on K_2CO_3–doped Li_4SiO_4–based pellets, Chem. Eng. J. 339 (2018) 51–60, https://doi.org/10.1016/j.cej.2018.01.117.

[15] P.W. Xiao, J.Y. Jun, J. Cheng, P.H. Zheng, P.X. Zhi, High–temperature adsorption of carbon dioxide on mixed oxides derived from hydrotalcite–like compounds, Environ. Sci. Tech. 42 (2008) 614–618, https://doi.org/10.1021/es072085a.

[16] L. Santamaría, S.A. Korili, A. Gil, Layered double hydroxides for CO_2 adsorption at moderate temperatures: synthesis and amelioration strategies, Chem. Eng. J. 455 (2023), 140551, https://doi.org/10.1016/j.cej.2022.140551.

[17] M. Salomé Macedo, M.A. Soria, L.M. Madeira, High temperature CO_2 sorption using mixed oxides with different Mg/Al molar ratios and synthesis pH, Chem. Eng. J. 420 (2021), 129731, https://doi.org/10.1016/j.cej.2021.129731.

[18] A.N. Narayanappa, P.V. Kamath, Interaction of pristine hydrocalumite-like layered double hydroxides with carbon dioxide, ACS Omega 4 (2019) 3198–3204, https://doi.org/10.1021/acsomega.9b00083.

[19] J.M. Silva, R. Trujillano, V. Rives, M.A. Soria, L.M. Madeira, High temperature CO_2 sorption over modified hydrotalcites, Chem. Eng. J. 325 (2017) 25–34, https://doi.org/10.1016/j.cej.2017.05.032.

[20] C.V. Miguel, R. Trujillano, V. Rives, M.A. Vicente, A.F.P. Ferreira, A.E. Rodrigues, A. Mendes, L.M. Madeira, High temperature CO_2 sorption with gallium–substituted and promoted hydrotalcites, Sep. Purif. Technol. 127 (2014) 202–211, https://doi.org/10.1016/j.seppur.2014.03.007.

[21] C. Rocha, M.A. Soria, L.M. Madeira, Effect of interlayer anion on the CO_2 capture capacity of hydrotalcite–based sorbents, Sep. Purif. Technol. 219 (2019) 290–302, https://doi.org/10.1016/j.seppur.2019.03.026.

[22] V. Rives, Layered double hydroxides, Nova Science Publishers Inc, New York, 2001.

[23] I. Rousselot, C. Taviot-Guého, F. Leroux, P. Léone, P. Palvadeau, J.P. Besse, Insights on the structural chemistry of hydrocalumite and hydrotalcite–like materials: Investigation of the series $Ca_2M3+(OH)6Cl·2H2O$ (M3+: Al3+, Ga3+, Fe3+, and Sc3+) by X–ray powder diffraction, J. Solid State Chem. 167 (2002) 137–144, https://doi.org/10.1006/jssc.2002.9635.

[24] A. Jiménez, R. Trujillano, V. Rives, M.Á. Vicente, Mixed–metal–oxide photocatalysts generated by high–temperature calcination of CaAlFe, hydrocalumite–LDHs prepared from an aluminum salt–cake, Catal. Today (2023) 114008.

[25] A. Jiménez, M. Valverde, A. Misol, R. Trujillano, A. Gil, M.Á. Vicente, Preparation of $Ca_2Al_{1-m}Fe_m(OH)_6Cl·2H_2O$–Doped hydrocalumites and application of their derived mixed oxides in the photodegradation of ibuprofen, ChemEng. 6 (2022) 64, https://doi.org/10.3390/chemengineering6040064.

[26] A. Jiménez, A. Misol, Á. Morato, V. Rives, M.A. Vicente, A. Gil, Optimization of hydrocalumite preparation under microwave irradiation for recovering aluminium

from a saline slag, Appl. Clay Sci. 212 (2021), 106217, https://doi.org/10.1016/j.clay.2021.106217.

[27] E. Pérez-Barrado, M.C. Pujol, M. Aguiló, Y. Cesteros, F. Díaz, J. Pallarès, L.F. Marsal, P. Salagre, Fast aging treatment for the synthesis of hydrocalumites using microwaves, Appl. Clay Sci. 80–81 (2013) 313–319, https://doi.org/10.1016/j.clay.2013.05.006.

[28] B. Paul, W. Chang, Mayenite–to–hydrocalumite transformation for the removal of chloride from salinized groundwater and the recycling potential of spent hydrocalumite for chromate removal, Desalination 474 (2020), 114186, https://doi.org/10.1016/j.desal.2019.114186.

[29] M. Hossein Beyki, M. Mohammadirad, F. Shemirani, A.A. Saboury, Magnetic cellulose ionomer/layered double hydroxide: An efficient anion exchange platform with enhanced diclofenac adsorption property, Carbohydr. Polym. 157 (2017) 438–446, https://doi.org/10.1016/j.carbpol.2016.10.017.

[30] Y. Takaki, X. Qiu, T. Hirajima, K. Sasaki, Removal mechanism of arsenate by bimetallic and trimetallic hydrocalumites depending on arsenate concentration, Appl. Clay Sci. 134 (2016) 26–33, https://doi.org/10.1016/j.clay.2016.05.010.

[31] C.F. Linares, J. Moscosso, V. Alzurutt, F. Ocanto, P. Bretto, G. González, Carbonated hydrocalumite synthesized by the microwave method as a possible antacid, Mater. Sci. Eng. C 61 (2016) 875–878, https://doi.org/10.1016/j.msec.2016.01.007.

[32] N. Murayama, I. Maekawa, H. Ushiro, T. Miyoshi, J. Shibata, M. Valix, Synthesis of various layered double hydroxides using aluminum dross generated in aluminum recycling process, Int. J. Miner. Process. 110–111 (2012) 46–52, https://doi.org/10.1016/j.minpro.2012.03.011.

[33] J. Granados-Reyes, P. Salagre, Y. Cesteros, Effect of the preparation conditions on the catalytic activity of calcined Ca/Al–layered double hydroxides for the synthesis of glycerol carbonate, Appl. Catal. A 536 (2017) 9–17, https://doi.org/10.1016/j.apcata.2017.02.013.

[34] J. Granados-Reyes, P. Salagre, Y. Cesteros, G. Busca, E. Finocchio, Assessment through FT–IR of surface acidity and basicity of hydrocalumites by nitrile adsorption, Appl. Clay Sci. 180 (2019), 105180, https://doi.org/10.1016/j.clay.2019.105180.

[35] M. Rosset, O.W. Perez-Lopez, Cu–Ca–Al catalysts derived from hydrocalumite and their application to ethanol dehydrogenation, React. Kinet. Mech. Catal. 126 (2019) 497–511, https://doi.org/10.1007/s11144-018-1513-y.

[36] R.L. Souza Júnior, T.M. Rossi, C. Detoni, M.M.V.M. Souza, Glycerol carbonate production from transesterification of glycerol with diethyl carbonate catalyzed by Ca/Al–mixed oxides derived from hydrocalumite, Biorefin. 13 (2023) 661–673, https://doi.org/10.1007/s13399-020-01110-4.

[37] B.R. Gevers, F.J.W.J. Labuschagné, Green synthesis of hydrocalumite (CaAl–OH–LDH) from Ca(OH)$_2$ and Al(OH)$_3$ and the parameters that influence its formation and speciation, Crystals 10 (2020) 672, https://doi.org/10.3390/cryst10080672.

[38] M. Sánchez-Cantú, C. Barcelos-Santiago, C.M. Gomez, E. Ramos-Ramírez, M.d.L. Ruiz Peralta, N. Tepale, V.J. González-Coronel, A. Mantilla, F. Tzompantzi, Evaluation of hydrocalumite-like compounds as catalyst precursors in the photodegradation of 2,4–dichlorophenoxyacetic acid, Int. J. Photoenergy 2016 (2016) 1–13.

[39] T.M. Rossi, J.C. Campos, M.M.V.M. Souza, An evaluation of calcined hydrocalumite as carbon dioxide adsorbent using thermogravimetric analysis, Appl. Clay Sci. 182 (2019), 105252, https://doi.org/10.1016/j.clay.2019.105252.

[40] H. Pfeiffer, T. Ávalos-Rendón, E. Lima, J.S. Valente, Thermochemical and cyclability analyses of the CO$_2$ absorption process on a Ca/Al Layered double hydroxide, J. Environ. Eng. 137 (2011) 1058–1065, https://doi.org/10.1061/(ASCE)EE.1943-7870.0000429.

[41] A. Jiménez, V. Rives, M.A. Vicente, A. Gil, A comparative study of acid and alkaline aluminum extraction valorization procedure for aluminum saline slags, J. Environ. Chem. Eng. 10 (3) (2022) 107546.

[42] Directive 2010/75/EU, 2022.

[43] A. Gil, S.A. Korili, Management and valorization of aluminum saline slags: current status and future trends, Chem. Eng. J. 289 (2016) 74–84, https://doi.org/10.1016/j.cej.2015.12.069.

[44] M. Yoldi, E.G. Fuentes-Ordoñez, S.A. Korili, A. Gil, Zeolite synthesis from industrial wastes, Microporous Mesoporous Mater. 287 (2019) 183–191, https://doi.org/10.1016/j.micromeso.2019.06.009.

[45] B.R. Das, B. Dash, B.C. Tripathy, I.N. Bhattacharya, S.C. Das, Production of η–alumina from waste aluminium dross, Miner. Eng. 20 (2007) 252–258, https://doi.org/10.1016/j.mineng.2006.09.002.

[46] L. Santamaría, L. Oliveira García, E.H. de Faria, K.J. Ciuffi, M.A. Vicente, S.A. Korili, A. Gil, M(II)–Al–Fe layered double hydroxides synthesized from aluminum saline slag wastes and catalytic performance on cyclooctene oxidation, Miner. Eng. 180 (2022), 107516, https://doi.org/10.1016/j.mineng.2022.107516.

[47] L. Santamaría, M. López-Aizpún, M. García-Padial, M.A. Vicente, S.A. Korili, A. Gil, Zn–Ti–Al layered double hydroxides synthesized from aluminum saline slag wastes as efficient drug adsorbents, Appl. Clay Sci. 187 (2020), 105486, https://doi.org/10.1016/j.clay.2020.105486.

[48] A. Gil, E. Arrieta, M.A. Vicente, S.A. Korili, Synthesis and CO$_2$ adsorption properties of hydrotalcite–like compounds prepared from aluminum saline slag wastes, Chem. Eng. J. 334 (2018) 1341–1350, https://doi.org/10.1016/j.cej.2017.11.100.

[49] L. Han, Q. Liu, Y. Zhang, Q. Wang, N. Rong, X. Liang, Y. Feng, K. Ma, M. Yan, Y. Hu, Catalytic toluene reforming with in situ CO2 capture via an iron-calcium hybrid absorbent for promoted hydrogen production, Energy Technol. 8 (2020) 1–12, https://doi.org/10.1002/ente.202000083.

[50] C. Rocha, M.A. Soria, L.M. Madeira, Doping of hydrotalcite–based sorbents with different interlayer anions for CO$_2$ capture, Sep. Purif. Technol. 235 (2020), 116140, https://doi.org/10.1016/j.seppur.2019.116140.

[51] M.K. Ram Reddy, Z.P. Xu, G.Q. Lu, J.C.D. Da Costa, Layered double hydroxides for CO$_2$ capture: structure evolution and regeneration, Ind. Eng. Chem. Res. 45 (2006) 7504–7509, https://doi.org/10.1021/ie060757k.

[52] A. Jiménez, M.A. Vicente, V. Rives, Thermal study of the hydrocalumite–katoite–calcite system, Thermochim. Acta. 713 (2022), 179242, https://doi.org/10.1016/j.tca.2022.179242.

[53] ICDD database. JCPDS – International Centre for Diffraction Data (ICDD®). Newton Square, PA, USA, (2022).

[54] S. Brunauer, P.H. Emmet, E. Teller, Adsorption of gases in multimolecular layers, J. Am. Chem. Soc. 60 (1938) 309–319, https://doi.org/10.1016/j.fuel.2016.10.086.

[55] M. Thommes, K. Kaneko, A.V. Neimark, J.P. Olivier, F. Rodriguez-Reinoso, J. Rouquerol, K.S.W. Sing, Physisorption of gases, with special reference to the evaluation of surface area and pore size distribution (IUPAC technical report), Pure Appl. Chem. 87 (2015) 1051–1069, https://doi.org/10.1515/pac-2014-1117.

[56] L.G. Joyner, E.P. Barrett, P. Halenda, The determination of pore volume and area distributions in porous substances. i. computations from nitrogen isotherms, J. Am. Chem. Soc. 73 (1951) 3155–3158, https://doi.org/10.1021/ja01151a046.

[57] X. Wang, C. Song, Carbon capture from flue gas and the atmosphere: a perspective, Front. Energy Res. 8 (2020), 560849, https://doi.org/10.3389/fenrg.2020.560849.

[58] A.C. Faria, R. Trujillano, V. Rives, C.V. Miguel, A.E. Rodrigues, L.M. Madeira, Alkali metal (Na, Cs and K) promoted hydrotalcites for high temperature CO$_2$ capture from flue gas in cyclic adsorption processes, Chem. Eng. J. 427 (2022), 131502, https://doi.org/10.1016/j.cej.2021.131502.

[59] R. Lide, CRC Handbook of Chemistry and Physics, 76th edition, 1995. doi: 10.1136/oem.53.7.504.

[60] J.D. Phillips, L.J. Vandeperre, Anion capture with calcium, aluminium and iron containing layered double hydroxides, J. Nucl. Mater. 416 (2011) 225–229, https://doi.org/10.1016/j.jnucmat.2010.11.101.

[61] G. Chen, S. Qian, X. Tu, X. Wei, J. Zou, L. Leng, S. Luo, Enhancement photocatalytic degradation of rhodamine B on nanoPt intercalated Zn–Ti layered double hydroxides, Appl. Surf. Sci. 293 (2014) 345–351, https://doi.org/10.1016/j.apsusc.2013.12.165.

[62] M. Maroño, Y. Torreiro, L. Gutierrez, Influence of steam partial pressures in the CO$_2$ capture capacity of K–doped hydrotalcite–based sorbents for their application to SEWGS processes, Int. J. Greenh. Gas Control 14 (2013) 183–192, https://doi.org/10.1016/j.ijggc.2013.01.024.

[63] E. López-Salinas, M.E.L. Serrano, M.A.C. Jácome, I.S. Secora, Characterization of synthetic hydrocalumite–type [Ca$_2$Al(OH)$_6$]NO$_3$·mH$_2$O: Effect of the calcination temperature, J. Porous Mater. 2 (1996) 291–297, https://doi.org/10.1007/BF00489810.

[64] M. Sánchez-Cantú, S. Camargo-Martínez, L.M. Pérez-Díaz, M.E. Hernández-Torres, E. Rubio-Rosas, J.S. Valente, Innovative method for hydrocalumite–like compounds' preparation and their evaluation in the transesterification reaction, Appl. Clay Sci. 114 (2015) 509–516.

[65] K. Gupta, S. Singh, M.S. Ramachandra Rao, Fast, reversible CO$_2$ capture in nanostructured Brownmillerite CaFeO$_{2.5}$, Nano Energy 11 (2015) 146–153, https://doi.org/10.1016/j.nanoen.2014.10.016.

[66] J.M. Silva, R. Trujillano, V. Rives, M.A. Soria, L.M. Madeira, Dynamic behaviour of a K–doped Ga substituted and microwave aged hydrotalcite–derived mixed oxide during CO$_2$ sorption experiments, J. Ind. Eng. Chem. 72 (2019) 491–503, https://doi.org/10.1016/j.jiec.2019.01.005.

[67] Martunus, Z. Helwani, A.D. Wiheeb, J. Kim, M.R. Othman, Othman, Improved carbon dioxide capture using metal reinforced hydrotalcite under wet conditions, Int. J. Greenh. Gas Control 7 (2012) 127–136.